SEASONALITY IN CARBON FLUX ATTENUATION EXPLAINS SPATIAL VARIABILITY IN TRANSFER EFFICIENCY

F. DE MELO VIRÍSSIMO[1,2,*], A. P. MARTIN[1], S. A. HENSON[1], J. D. WILSON[3,4]

[1] *National Oceanography Centre, Southampton, SO14 3ZH, United Kingdom*
[2] *Grantham Research Institute on Climate Change and the Environment, London School of Economics and Political Science, London, WC2A 2AE, United Kingdom*
[3] *School of Earth Sciences, University of Bristol, Bristol, BS8 1QU, United Kingdom*
[4] *Department of Earth, Ocean and Ecological Sciences, University of Liverpool, Liverpool, L69 3GP, United Kingdom*

NOTE: THIS IS A NON-PEER REVIEWED PREPRINT SUBMITTED TO EARTHARXIV

Abstract. Each year, the biological carbon pump is responsible for converting carbon dioxide into millions of tonnes of organic carbon, and for transferring a fraction of it to the deep ocean, where it can remain for hundreds of years. The efficiency of this surface-to-depth carbon transfer varies geographically, and is a key determinant of the atmosphere-ocean carbon dioxide balance. Traditionally, the attention has been focused on explaining perceived geographical variation in an attempt to understand it, an approach that has led to conflicting results. Here we use a combination of observations and modelling to show that the spatial variability in transfer efficiency can instead be due to seasonal variability in carbon flux attenuation. We also show that seasonality can explain the contrast between known global estimates of transfer efficiency, due to differences in the date and duration of sampling, as well as the methodologies used to derive the estimates. Our results suggest caution in the mechanistic interpretation of annual-mean patterns in transfer efficiency and demonstrates that seasonally and spatially-resolved datasets are required to generate accurate evaluations of the biological carbon pump.

Keywords: biological carbon pump, carbon transfer efficiency, seasonality in flux attenuation, mesopelagic ocean, sinking speed, remineralisation

*Corresponding Author. e-mail: f.de-melo-virissimo@lse.ac.uk.

Author contributions: F.d.M.V. designed the study and performed all simulations and analyses. J.D.W. produced Fig. S1. F.d.M.V. wrote the manuscript with input from A.P.M., S.A.H. and J.D.W.

The authors declare no conflict of interest.

Introduction

The biological carbon pump (BCP) plays a crucial role in the ocean's carbon cycle by removing large quantities of carbon dioxide (CO_2) from the surface ocean to the deep interior [1]. In this process, marine phytoplankton assimilate dissolved CO_2 in the sunlit, upper ocean to produce around 50 Pg of organic carbon per year [2]. While most organic carbon production is quickly respired back into inorganic carbon, about 10-20% leaves the upper ocean (is "exported") [3] as particulate organic carbon (POC), or detritus, from surface waters into the mesopelagic ocean (100-1,000m). Eventually, part of this POC reaches the deep, bathypelagic ocean (below 1,000m), where it may remain for hundreds of years [4] before returning to the surface ocean as dissolved inorganic carbon (DIC). Through this process, the BCP is estimated to sequester over 1,280 Pg C at steady state [5], and in this way lowering the baseline atmospheric concentration of CO_2 by more than 50% with respect to the effects of physical and chemical equilibrium alone [6].

In this biogeochemical journey, there are essentially two contrasting processes which determine the fate of the exported POC: sinking and remineralisation [7]. As POC sinks downward, it is remineralised by being broken down and respired by heterotrophic organisms. It is the balance between these processes (which may also include coupling [8]) that determines the efficiency of the BCP in transferring POC to the deep ocean. For a given remineralisation rate, the faster the POC sinks, the more of it will survive the journey, with a higher fraction reaching the deep ocean. The 'transfer efficiency' (hereafter TE) is defined as the ratio between the POC flux at 1,000m divided by the export flux.

In practice, TE is usually derived from particle flux profiles by applying a function to describe the decrease of flux with depth; the most popular function is the "Martin curve" [9, 7]. This formulation states that TE equals the ratio of the export depth and the transfer depth to the power of an exponent, hereafter b, where the exponent b can be estimated from flux profiles (Supporting Information). From a mechanistic point of view, b can be expressed as the ratio between sinking and remineralisation rates (Equation (8) in Supporting Information). For this reason, b is usually referred to as the flux attenuation exponent. Since the proposal of such parameterisations for the BCP, they have been widely used in both data and model-based studies, often with the flux attenuation exponent assuming Martin's original value of $b = 0.858$ [9].

Evidence from observation and model-based studies suggest the flux attenuation exponent, and therefore TE, is significantly variable. For instance, a series of independent field-based investigations [10, 11, 12, 13, 14] estimated values of b between 0.5 and 2.0 across the ocean, later used as the basis to assess the influence of remineralisation depth changes on atmospheric pCO_2 [15, 16]. Several global compilations for TE to be proposed over the years, with two of them standing out: a compilation of Thorium-derived export fluxes and sediment-trap fluxes at 2,000m [17], which found TE to be lower at low latitudes and high at high latitudes, and a compilation obtained from a limited set of eight data points collected with neutrally-buoyant mesopelagic sediment-traps from the North Atlantic and Pacific, which showed the opposite pattern [18]. Later studies using data-constrained modelling [19, 20, 21] obtained TE distributions that agreed with the latter, but were not able to explain why they differ from the former. It is important to understand the source of such variability because the spatial patterns can be used to infer net dominant processes such as temperature-dependent remineralisation or ballasting, which can then be used to make predictions of how carbon sequestration by the BCP may change as a response to climate-driven changes in those processes [16].

More recently, additional evidence for seasonal variability in TE has been presented [22, 23, 24], with subsequent implications for carbon sequestration. Numerical experiments show that addition of seasonal variability of 60% (about the mean) in the flux attenuation parameter more than doubles the sequestration of carbon predicted by an ocean-biogeochemical model [25].

Here, we demonstrate the importance of resolving seasonality in the BCP with three key results: first, we leverage from an extensive data compilation of POC flux attenuation parameter values [26] to constrain the mean seasonal cycle in each hemisphere, which is shown to approximate a cosine curve as presented in Figs. 1 and S.1. We then use a global ocean-biogeochemical model to link seasonal to spatial variability by showing that the presence of a seasonally-varying but spatially uniform flux attenuation is, by itself, sufficient to generate spatial variability in TE, with a resulting global distribution of annual TE that agrees with those presented in the literature [18, 19, 20, 21]. Finally, we show that considering seasonality allows the reconciliation of the conflicting results for global annual TE spatial patterns discussed above [17, 18].

In what follows, we apply a uniform but seasonally-varying flux attenuation informed by sediment-trap observations (Figs. 1, S.1 and S.2) within a coupled global ocean-biogeochemical model. To allow a direct comparison between the constant and seasonal flux attenuation scenarios, as well as to remove uncertainties when computing TE, we assume that the POC is not transported by circulation and can only sink vertically. A detailed description of the model and underlying assumptions is presented in the Materials and Methods section and the Supporting Information.

Seasonality leads to spatial variability in annual transfer efficiency

In the absence of seasonal variability in the model's flux attenuation b^{model} and sinking speed (see Materials and Methods and Supporting Information), the annual mean TE is spatially invariant throughout the ocean†. This is shown in Fig. S.3 (Supporting Information) for the model's original value of $b^{\text{model}} = 1.388$, which means that TE ≈ 0.04738 as predicted by the Martin curve (see Supporting Information). When seasonality in attenuation and sinking speed is present (Fig. 2(a)), the annual mean TE is no longer homogeneous and shows a broad spatial pattern of values ranging from approximately 0.15-0.3 in the Southern Ocean, North Atlantic and North Pacific, and 0.05-0.15 in the subtropical gyres and tropical areas. The consistent spatial pattern of high TE at high latitudes and low at low latitudes, particularly in the subtropics, is in agreement with previous attempts to estimate TE using a variety of methods such as data-constrained modelling [19, 20], large-scale mechanistic modelling [21] and from neutrally-buoyant sediment traps [18]. The exception is the pattern obtained from deep-sea sediment and Thorium-derived export fluxes compilation analysis [17], which found TE to be higher in low latitudes than in high latitudes, a conclusion that we will examine further in the next section.

The annual mean TE in ocean provinces (Fig. 2(b); see Supporting Information for the provinces division and flux calculations) shows that the Antarctic province AAZ and North Atlantic province NA have high values of TE (0.18 and 0.16 respectively), while the subtropical provinces STA and STP have the lowest values of 0.13 and 0.11 respectively, with all other provinces showing values in between. These estimates are in good qualitative agreement with previous modelling studies [21] and within the uncertainty margin of data-constrained modelling studies [19, 20] for all provinces but STP and NP in the Pacific Ocean, with the caveat that our province division is similar but slightly different (see Supporting Information). The annual global mean TE is 0.14, which also falls between the high and low latitude values in Fig. 2(a). However, it is slightly lower than the 0.15 given by the Martin curve when $b = 0.858$.

The emergence of a spatial pattern in TE in the model, despite having a spatially-homogeneous flux attenuation, is a direct consequence of the seasonal variability in the attenuation. If the attenuation is invariant throughout the year, its effect on the sinking detritus concentrations (and fluxes) is simply to reduce the concentration of detritus with depth, but keeping the shape of the time series unchanged (Fig. 3(a)), like a travelling wave under damping. Therefore, at different depths, the detritus concentration has the same seasonal cycle, but with an increasing lag relative to the export depth, as illustrated for a location in the South Atlantic in Fig. 3(c). Because this attenuation is constant at all locations, the ratio between the 1-year integral of the time series at any two depths below the export depth will be the same at any location (Fig. 3(a)). If seasonality is present, the differing attenuation at different times of the year will alter the time series of flux at depth: for example, periods of higher flux from the surface may coincide with low attenuation in some locations, but with high attenuation in others. The deeper the depth horizon considered, the greater the lag with respect to the time series at the export depth, as shown in Fig. 3(b) and Fig. 3(d). As this distortion is dependent on the characteristics of the time series, the ratio between the 1-year integral of the time series at two depths below the export depth will be different at different locations. Examples of modelled time series in the Pacific and Indian Oceans are shown in Supporting Information.

The results in Figs. 2 and 3 demonstrate that spatial variability in TE may not emerge uniquely from spatially-varying processes, such as temperature-dependent remineralisation, but could also arise from the coupling between seasonally-varying processes, therefore challenging the interpretation of spatial variability in annual mean TE datasets.

Seasonality reconciles contrasting spatial patterns of observed transfer efficiency

The seasonal variability in attenuation can also explain apparent conflicts between existing estimates for TE [18, 19, 20, 21, 17, 26]. The existence of a seasonal cycle itself implies that if sampling the same location in the ocean at different times of the year, estimates of flux attenuation and TE are likely to be quite different. In addition, the seasonal cycle could be highly episodic: as ship-board observations are collected for very short periods, sampling might occur in e.g. an overall period of slow sinking with occasional short-lived peaks. Hence, compiling short-duration observations from several years made at different times of the year and at different locations assuming they represent a single snapshot of the ocean BCP state is likely to be misleading.

Previous suggestions [18] on how to reconcile these divergent estimates focused on the possibility of a fast upper mesopelagic attenuation followed by slow attenuation in the deep ocean in warm waters, with the converse happening in cold waters, but did not consider the role of seasonality and variability in flux attenuation and sinking speeds, nor the implicit steady-state assumption that is inherent in most reports of short-term observations of sinking POC [27]. Although this temperature-attenuation relationship was later observed in a data-constrained model analysis [20], the existence of this phenomenon was not enough to generate the high-latitude low-TE patterns [20].

Here we argue that the different time scales introduced by temporal variability of attenuation and sinking provides an explanation for the high-latitude low-TE pattern. In a situation where flux attenuation varies seasonally, sufficiently frequent sampling to allow representation of global annual averages is not typically viable with ship-based observations.

To test whether this mechanism could provide an answer to the contrasting pattern of TE obtained in the study using sediment trap and Thorium-derived

†Note that, after spinup, the cycle is quasi-periodic and not 100% periodic.

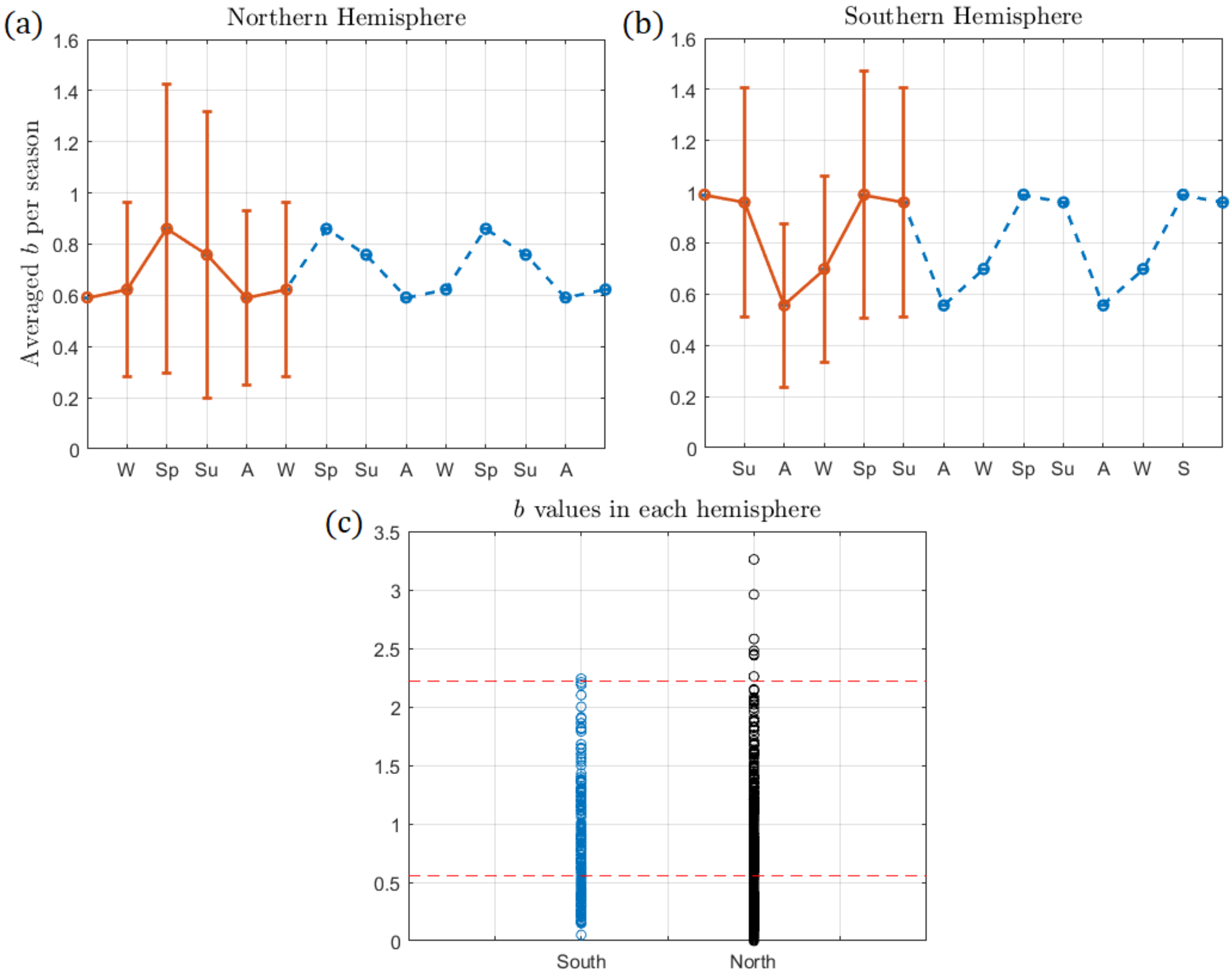

Figure 1: Constraining the seasonal cycle in the flux attenuation paramater b in each hemisphere from the dataset [26]. Top left: (a) Seasonally averaged flux attenuation parameter b in the Northern Hemisphere. The solid red line shows one full seasonal cycle, while the blue dash line shows the cycle repeated, to highlight its sinusoidal pattern. The error bars shows one standard deviation from the mean. Top right (b) Seasonally averaged flux attenuation parameter b in the Southern Hemisphere, with the description as in (a). Bottom (c): Distribution of b values from the dataset in each hemisphere. The dashed red line highlights the values of $b = 0.555$ and $b = 2.221$ (the minimum and maximum values used in this study).

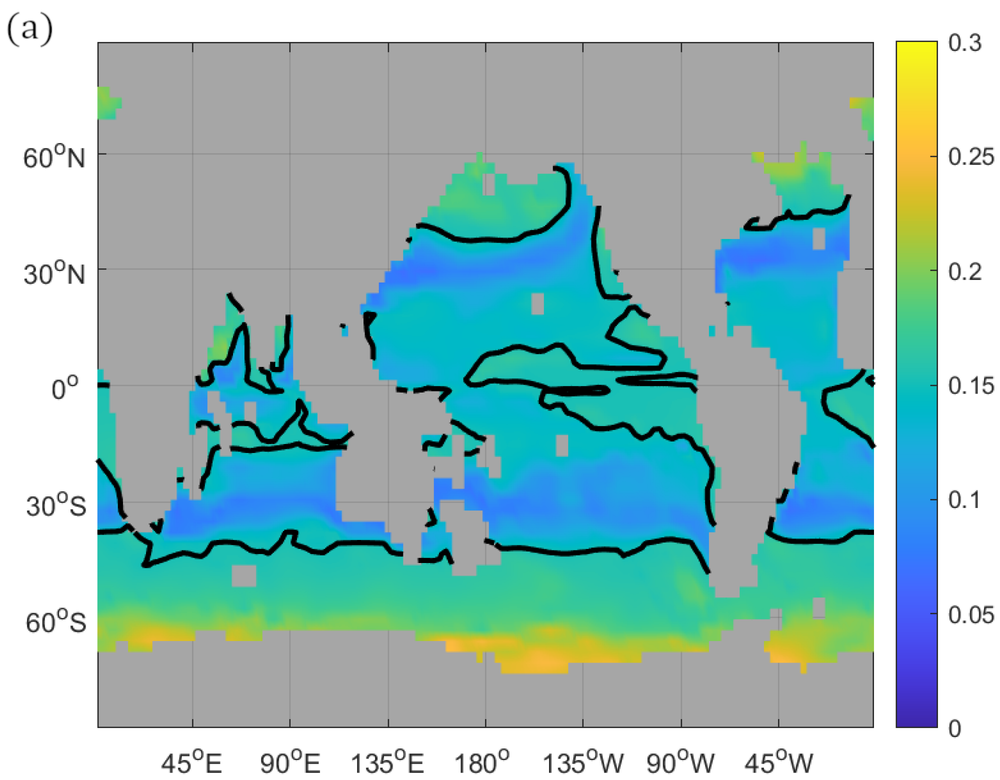

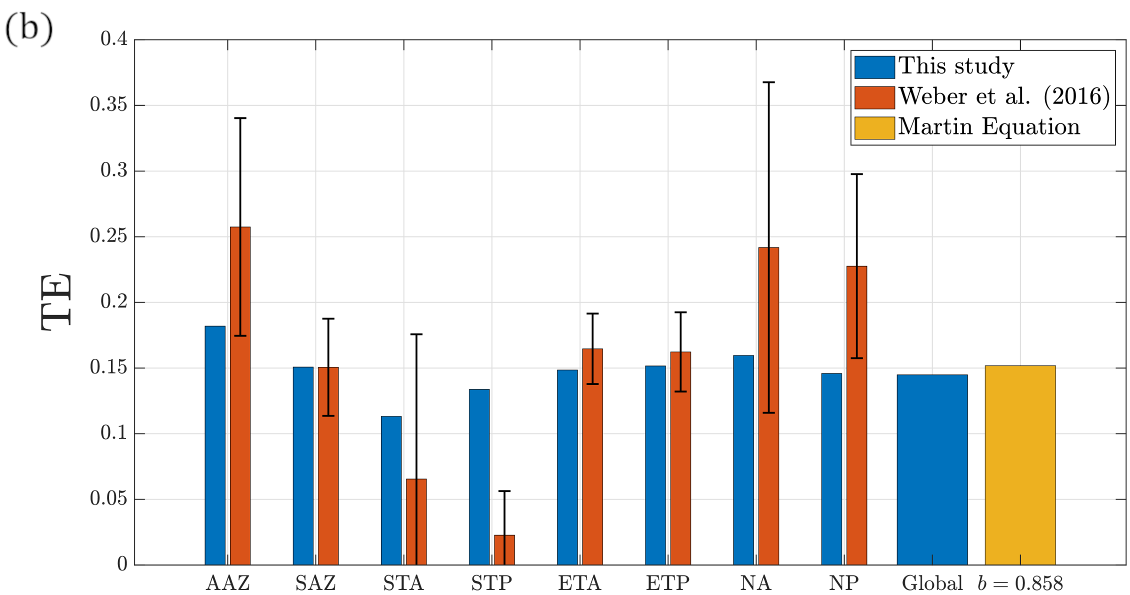

Figure 2: Annual mean transfer efficiency (TE), when detritus is not transported by the ocean circulation. Top: (a) TE for a seasonal b^{model} - the solid black contour lines represents the TE computed from the Martin curve for $b = 0.858$. Bottom: (b) annual mean TE in each ocean province (definition in the Supplementary Materials) using data from this study (blue bars) and the data-constrained modelling study [19] (red bars, with intervals indicating the uncertainty in their analysis), with the yellow bar showing the value for TE as estimated using the Martin curve (Supplementary Materials) for $b = 0.858$. Note that the province definition in this study and in the data-constrained modelling study [19] are slightly different (see Supplementary Materials).

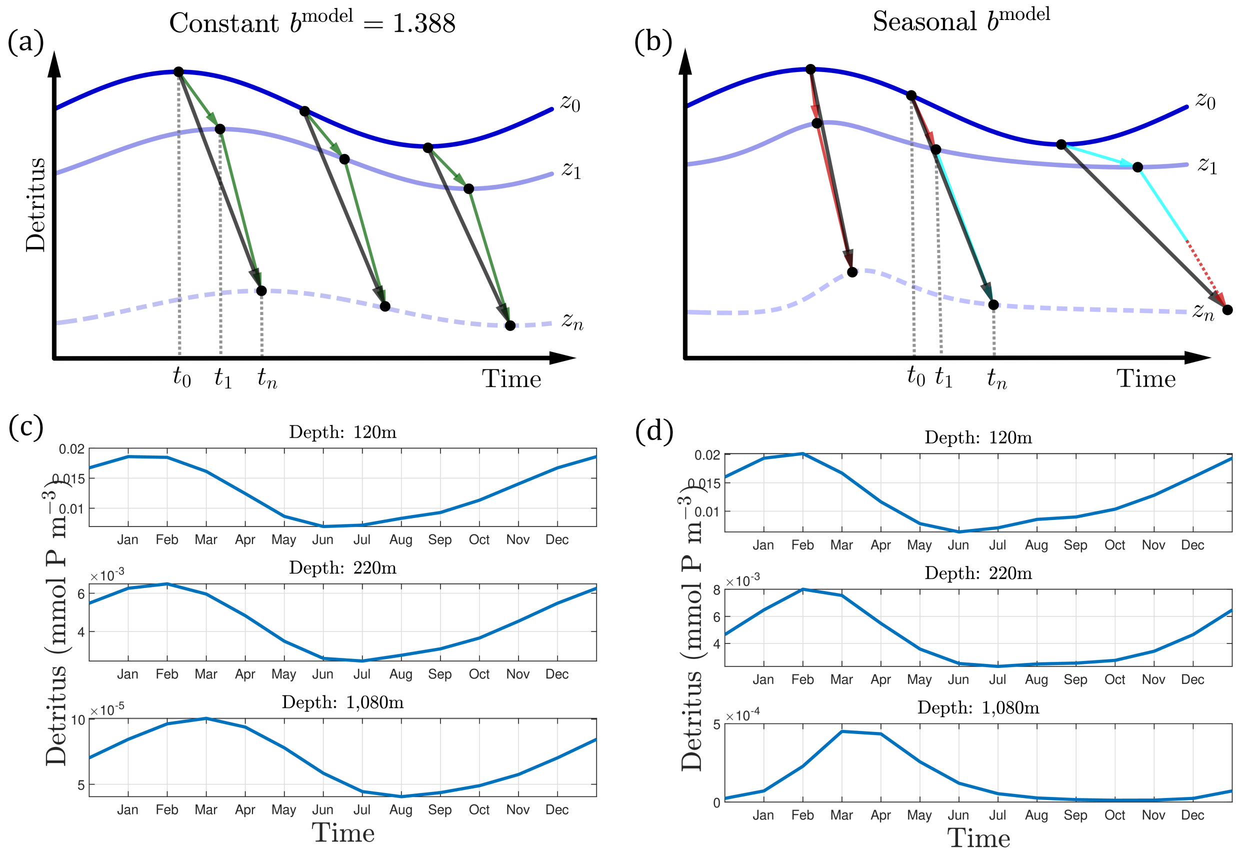

Figure 3: Exported detritus attenuation in constant and seasonal attenuation scenarios, when detritus is not transported by the ocean circulation. Top: schematic representation showing how detritus is attenuated in a non-seasonal scenario (a) and when seasonality is present (b). In (a), detritus that is at the export depth z_0 at an instant t_0 would be uniformly attenuated, reaching a depth z_1 at an instant t_1, as shown by the green arrow. Then, the attenuation continues at an uniform rate, with sinking speed increasing as a function of depth, so that the remaining detritus reaches the transfer depth z_n at an instant t_n. As both attenuation and sinking are constant in time, this process is independent of the starting point, as shown by the dark grey arrows, which are parallel to each other. In (b), the attenuation varies seasonally and hence the journey of detritus is dependent on time of the year. For instance, detritus that is at the export depth z_0 at the instant t_0 depicted would go through a lower attenuation, sinking at a faster rate until it reaches z_1 at the instant t_1, as shown by the red arrow. This is then followed by a faster attenuation, when detritus sinks at a slower rate, until it reaches the transfer depth z_n at an instant t_n, as shown by the light blue arrow. For detritus leaving z_0 at other times, the attenuation journey would be different, and hence the grey arrows are not parallel. Bottom: modelled time series for detritus concentration in the South Atlantic (43.59°S, 29.53°W) at different depths for a constant $b^{\text{model}} = 1.388$ (c) and a seasonal b^{model} (d), demonstrating the phenomena described in (a) and (b) respectively. Note the changing scale of the y-axes in panels (c) and (d).

fluxes observations [17], we reproduced their sampling methodology as closely as possible from our model simulations, given the limitations of our modelling framework (see Supporting Information).

Fig. 4 shows the results of reproducing the sediment trap and Thorium-derived fluxes study [17] using the same model data used to produce Fig. 2. Instead of computing the annual average export and transfer flux to produce a TE map as in Fig. 2(a), we sampled the model data at locations and times that best matched their approach (see Supporting Information for details). Specifically, we randomly sampled a total of 150 high and low latitude locations shown in Fig. 4(a), from which we took annual fluxes at 1,000m and seasonally averaged fluxes at 120m, with the corresponding mean surface (0-120m) temperature for the same period. We then used these data to compute TE at each sampled location, which was correlated (both linearly and exponentially, see Supplementary Materials) with the surface mean temperature at the same location, as shown in Fig. 4(b). This process was repeated 10,000 times to quantify the uncertainty, giving a normally-distributed R^2 with mean 0.79 and variance 0.033 for the exponential regression (see Supplementary Materials). The mean correlation maps (linear and exponential) were then used to produce global TE maps. The resulting map for the exponential fit is shown in Fig. 4(b) (see Supplementary Materials for the linear fit map). This provides a fairly reasonable explanation to the differences with the sediment trap-based study [18], showing a low TE in high latitudes and a higher TE in the tropics and subtropics, hence suggesting that the seasonal signal for export in these periods were enough to reverse the TE pattern from Fig. 2(a) - even though both TE maps were generated from the same data. A similar result was obtained when using the mean upper-mesopelagic (120-540m) temperature, which is shown in the Supplementary Materials.

Our analysis demonstrates that temporally-inconsistent data compilations could lead to differing conclusions, particularly when generalised to non-sampled parts of the ocean. In this case, measurements that have some consistency in date (i.e. from around the same time of the year) and location might be required to draw robust conclusions on the processes driving the BCP.

Caveats in this study

This study has some caveats, which are informative and offer opportunities for further investigations. These include the use of a coarse resolution model which does not resolve small scale processes (although they are parameterised), as well as a periodically-repeating circulation. However, we note that these methods have been successfully employed in a variety of studies [28, 29, 19, 20, 30].

Another limitation is in the use of a non-mechanistic seasonal cycle in flux attenuation, which is based on very limited evidence [26], and is the simplest representation of seasonal variation in attenuation. In reality, it may vary in both amplitude and phase with location, but the details are still uncertain. The shape (i.e. how peaked) of the attenuation time series might, at some locations, be quite different from the simple smooth signal (see Materials and Methods) considered in this work. Although the true shape could be different, this does not affect the main results. The important feature is the lag between POC export and attenuation which is where we believe the scientific attention should now focus.

The results in this study also ignore the effects, albeit small, of circulation in the transport of detritus, meaning that it can only move vertically due to gravity, but is not transported laterally. This is only a minor hypothesis which has been deliberately used in other studies [31], and in the diagnostics of b in the data-constrained modelling study [19]. However, adding the effect of the circulation in the advection of would change slightly the fluxes and introduce minor spatial patterns in TE [25], therefore preventing a clean diagnostic of the contribution due to the presence of seasonality. Furthermore, this hypothesis has two important benefits: first, it demonstrates this effect can take place even with strictly local influence; Second, this approach removes any uncertainties when quantifying the ratio of fluxes at two depths in a single location (where the deeper one may average a larger area in reality).

These model limitations, however, do not affect the purpose of this study, which is not to reproduce reality *ipsis literis* but to test a hypothesis and demonstrate a phenomenon. Hence, it should not be taken as an intended accurate depiction of the real seasonal cycle, nor be reproduced in models as such, despite being successful in reconciling previous literature results while highlighting an important but neglected phenomenon. Note that it also ignores the fact that a real flux attenuation time series might show inter-annual variability, and hence its scope is limited to the hypothesis tested in this study.

Summary and conclusion

We showed that the addition of a seasonal cycle in the flux attenuation has at least three striking consequences for the global patterns of annual TE. First, spatial variability is generated despite both flux attenuation and sinking speed being spatially homogeneous at each instant of time. Second, the emerging spatial pattern in annual TE is highly similar to that reported in the literature [18, 19, 20, 21]. Third, accounting for the seasonality allows for the high-latitude high-TE map [18] to be reconciled with the alternative high-latitude low-TE pattern [17].

These results suggest that seasonal variability in flux attenuation and sinking speed is a route for generating spatial variability in annual TE, as a natural emerging property of the system dynamics. This is dif-

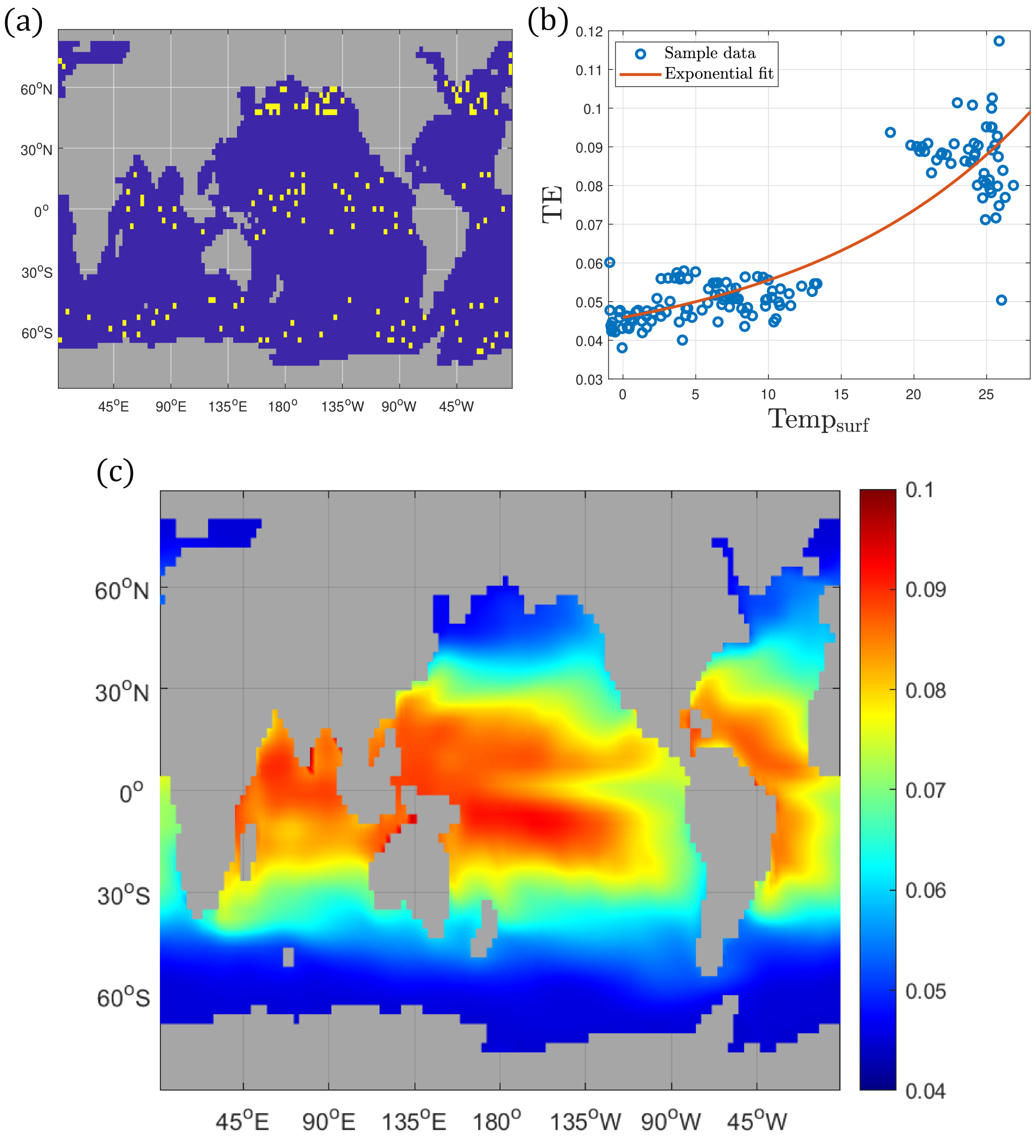

Figure 4: Time-discrete sampling with seasonal variability in attenuation can produce contrasting spatial patterns in the true annual mean TE shown in Fig. 2(a), providing an explanation to reconcile previous sediment trap studies [17, 26]. Top: (a) export and transfer fluxes were sampled randomly, and (b) a nonlinear (exponential) regression of the resulting TE against the surface (0-120m) temperature was performed. This procedure was repeated 10,000 times and the resulting parameterisation was used to compute the TE map shown in panel (c).

ferent from imposing a spatially-varying TE or b^{model} *a priori*, and is the simple consequence of the coupling between two seasonal time series (i.e. flux attenuation and export of organic material; or equivalently, sinking speed and detritus concentration) to obtain fluxes - excluding the transport due to circulation.

This has also implications for CMIP-class models run under anthropogenic forcing: changes in climate forcing might trigger changes in the seasonal cycle and hence impact carbon fluxes and spatial variability in TE too. Hence, assuming a fixed spatial and temporal pattern in flux attenuation limits the model assessment of the BCP and sequestration under climate change in the IPCC scenarios. This is particularly important as previous numerical studies have demonstrated that changes in the phase impact the amount of carbon that is transferred to the deep ocean [25], meaning that we need to understand the causes of the lag between POC export and attenuation to have more confidence in predictions. We note that most CMIP6 models adopt constant (in time, space and depth) sinking speeds [32, 33], with only two models using a variable formulation: one has a sinking speed that is constant in time but increases with depth [34], and another has a sinking speed that varies according to the nutrient stress [35]. Therefore, incorporating mechanistic-based models for sinking particles is an open challenge for the CMIP7 generation and beyond.

Finally, observationally resolving the temporal scales of fluxes and related processes such as sinking speed, remineralisation, and metabolic rates would represent a big step towards a better quantification and understanding of the BCP, and particularly the seasonality of export and attenuation. Model estimates of flux are difficult to validate due to sparsity of observations [19], not only spatially but especially temporally, but there is a potential for autonomous observations to fill in some of the gaps - particularly the seasonal variability in attenuation [36, 22, 37, 38, 39]. In addition, the use of data-constrained models and machine learning [40] offer some hope and can be a fruitful avenue to extract seasonal information from the more abundant data existent for other tracers and processes, and should be one of the top priorities for the biogeochemical and climate modelling communities over the next few years.

Materials and methods

Diagnostic model

We use a coupled global ocean-biogeochemical model. The biogeochemical component is the GEOMAR NPZD-DOP model [41, 42]. The biogeochemistry is coupled to the circulation via a transport-matrix (TMM) framework [43, 28, 44]. For the circulation, we use 12 monthly averaged transport matrices derived from the MITgcm 2.8° [43, 44]. This model includes detritus explicitly as a tracer, which sinks at an intrinsic speed $w(z) = a \cdot z$ m day^{-1}, $a > 0$, and is remineralised at a constant rate $\lambda = 0.05$ day^{-1}. In the absence of circulation, the 1-year average fluxes are given by the Martin curve, with $b = \lambda/a$. To avoid confusion with the Martin curve, we denote the model's flux attenuation by b^{model} [25]. With the TMM, it is also possible to easily turn off circulation influence on detritus, and hence remove its effect on detritus transport [25], this way allowing for a clean diagnostic of the effects of a seasonal flux attenuation. The latter is a crucial point in this study and, in all simulations, the ocean circulation does not act on the sinking detritus (but does act on all other tracers).

Seasonal cycle

The model has been modified to incorporate seasonality in its flux attenuation by modifying its sinking speed: since $a = \lambda/b^{\text{model}}$, we replace b^{model} by a seasonally-varying version constrained by observations [26] as per Figs. 1 and S.1. This seasonal b^{model} has variability of 60% around the model's original reference value of $b^{\text{model}} = 1.388$, as shown in Fig. S2 (Supporting Information). This covers the range of observed values from about 0.5 to 2.0 [15], as shown in Fig. 1(c), while excluding very low values (below 0.5) which, in our model, would lead to unrealistically fast sinking of POC. The phase (with respect to 1st of January) was also constrained from observations, as shown in Figs. 1(a,b), and is approximately 3 months ahead of growth rate of phytoplankton and solar radiation (Supporting Information). The former means that fastest sinking (lowest attenuation and highest transfer efficiency) happens between February and May, which occurs about 3 months after maximum growth (as suggested by North Atlantic glider data [22]). This phase is also within the uncertainty margin reported from annual sediment trap data for the North Red Sea [23]. Note that the seasonal b^{model} is spatially homogeneous at each instant of time, so there is no spatial variability in b^{model} nor in sinking speed at each depth.

Model data

All model output used in this work is freely available online on Zenodo [45]. The flux attenuation data used to generate Fig. 1 is available as supplementary materials in the referred manuscript [26]. The data [19] used to generate Fig. 2(b) is available on Bitbucket [21, 46]. All figures in this work were generated by the authors, except the aforementioned Fig. 2(b), which includes data from the data-constrained modelling study [19] published by others [21]. Fig. 3(a) and Fig. 3(b) were generated using the software GeoGebra [47]. Fig. S1 was generated using the MATLAB package M_map [48].

Acknowledgements

This work was funded by: an European Research Council Consolidator grant (GOCART, agreement number 724416) in support of F.d.M.V. and S.A.H.; by a Large Grant from the UK Natural Environment Research Council (COMICS, agreement numbers NE/M020835/1 and NE/M020835/2) in support of F.d.M.V., A.P.M. and S.A.H.; and by a UK Natural Environment Research Council RoSES programme grant (CUSTARD, agreement number NE/P021247/2) in support of F.d.M.V., A.P.M. and S.A.H. J.D.W. acknowledges support from the AXA Research Fund.

References

[1] Tyler Volk and Martin I. Hoffert. *Ocean Carbon Pumps: Analysis of Relative Strengths and Efficiencies in Ocean-Driven Atmospheric CO2 Changes*, pages 99–110. American Geophysical Union (AGU), 2013.

[2] I. D. Lima, P. J. Lam, and S. C. Doney. Dynamics of particulate organic carbon flux in a global ocean model. *Biogeosciences*, 11(4):1177–1198, 2014.

[3] Grace K. Saba, Adrian B. Burd, John P. Dunne, Santiago Hernández-León, Angela H. Martin, Kenneth A. Rose, Joseph Salisbury, Deborah K. Steinberg, Clive N. Trueman, Rod W. Wilson, and Stephanie E. Wilson. Toward a better understanding of fish-based contribution to ocean carbon flux. *Limnology and Oceanography*, 66(5):1639–1664, 2021.

[4] Tim DeVries, Francois Primeau, and Curtis Deutsch. The sequestration efficiency of the biological pump. *Geophysical Research Letters*, 39(13), 2012.

[5] Michael Nowicki, Tim DeVries, and David A. Siegel. Quantifying the carbon export and sequestration pathways of the ocean's biological carbon pump. *Global Biogeochemical Cycles*, 36(3):e2021GB007083, 2022. e2021GB007083 2021GB007083.

[6] E. Maier-Reimer, U. Mikolajewicz, and A. Winguth. Future ocean uptake of CO_2: interaction between ocean circulation and biology. *Climate Dynamics*, 12:711–722, 1996.

[7] Jack J. Middelburg. *Marine Carbon Biogeochemistry: A Primer for Earth System Scientists*. Springer International Publishing, 1st edition, 2019.

[8] U. Alcolombri, F.J. Peaudecerf, V.I. Fernandez, L. Behrendt, K. Soo Lee, and R. Stocker. Sinking enhances the degradation of organic particles by marine bacteria. *Nature Geosciences*, 14:775–780, 2021.

[9] John H. Martin, George A. Knauer, David M. Karl, and William W. Broenkow. Vertex: carbon cycling in the northeast pacific. *Deep Sea Research Part A. Oceanographic Research Papers*, 34(2):267 – 285, 1987.

[10] William M. Berelson. The flux of particulate organic carbon into the ocean interior: A comparison of four u.s. jgofs regional studies. *Oceanography*, 14:59–67, 2001.

[11] Ken O. Buesseler, Carl H. Lamborg, Philip W. Boyd, Phoebe J. Lam, Thomas W. Trull, Robert R. Bidigare, James K. B. Bishop, Karen L. Casciotti, Frank Dehairs, Marc Elskens, Makio Honda, David M. Karl, David A. Siegel, Mary W. Silver, Deborah K. Steinberg, Jim Valdes, Benjamin Van Mooy, and Stephanie Wilson. Revisiting carbon flux through the ocean's twilight zone. *Science*, 316(5824):567–570, 2007.

[12] Maureen H Conte, Nate Ralph, and Edith H Ross. Seasonal and interannual variability in deep ocean particle fluxes at the oceanic flux program (ofp)/bermuda atlantic time series (bats) site in the western sargasso sea near bermuda. *Deep Sea Research Part II: Topical Studies in Oceanography*, 48(8):1471–1505, 2001.

[13] Roger Francois, Susumu Honjo, Richard Krishfield, and Steve Manganini. Factors controlling the flux of organic carbon to the bathypelagic zone of the ocean. *Global Biogeochemical Cycles*, 16(4):34–1–34–20, 2002.

[14] Michael Lutz, Robert Dunbar, and Ken Caldeira. Regional variability in the vertical flux of particulate organic carbon in the ocean interior. *Global Biogeochemical Cycles*, 16(3):11–1–11–18, 2002.

[15] E. Kwon, F. Primeau, and J. Sarmiento. The impact of remineralization depth on the air–sea carbon balance. *Nature Geosciences*, 2:630–635, 2009.

[16] J. D. Wilson, S. Barker, N. R. Edwards, P. B. Holden, and A. Ridgwell. Sensitivity of atmospheric co2 to regional variability in particulate organic matter remineralization depths. *Biogeosciences*, 16(14):2923–2936, 2019.

[17] Stephanie A. Henson, Richard Sanders, and Esben Madsen. Global patterns in efficiency of particulate organic carbon export and transfer to the deep ocean. *Global Biogeochemical Cycles*, 26(1), 2012.

[18] Chris M. Marsay, Richard J. Sanders, Stephanie A. Henson, Katsiaryna Pabortsava, Eric P. Achterberg, and Richard S. Lampitt. Attenuation of sinking particulate organic carbon flux through the mesopelagic ocean. *Proceedings of the National Academy of Sciences*, 112(4):1089–1094, 2015.

[19] Thomas Weber, Jacob A. Cram, Shirley W. Leung, Timothy DeVries, and Curtis Deutsch. Deep ocean nutrients imply large latitudinal variation in particle transfer efficiency. *Proceedings of the National Academy of Sciences*, 113(31):8606–8611, 2016.

[20] Tim DeVries and Thomas Weber. The export and fate of organic matter in the ocean: New constraints from combining satellite and oceanographic tracer observations. *Global Biogeochemical Cycles*, 31(3):535–555, 2017.

[21] Jacob A. Cram, Thomas Weber, Shirley W. Leung, Andrew M. P. McDonnell, Jun-Hong Liang, and Curtis Deutsch. The role of particle size, ballast, temperature, and oxygen in the sinking flux to the deep sea. *Global Biogeochemical Cycles*, 32(5):858–876, 2018.

[22] Roséanne Bol, Stephanie A. Henson, Anna Rumyantseva, and Nathan Briggs. High-frequency variability of small-particle carbon export flux in the northeast atlantic. *Global Biogeochemical Cycles*, 32(12):1803–1814, 2018.

[23] Stephanie. S. Kienast and Adi Torfstein. Evaluation of biological carbon pump metrics in the subtropical gulf of aqaba, northern red sea. *Global Biogeochemical Cycles*, 36(10):e2022GB007452, 2022. e2022GB007452 2022GB007452.

[24] Stephanie A. Henson, Nathan Briggs, Filipa Carvalho, Clara Manno, Alexandre Mignot, and Sandy Thomalla. A seasonal transition in biological carbon pump efficiency in the northern scotia sea, southern ocean. *Deep Sea Research Part II: Topical Studies in Oceanography*, 208:105274, 2023.

[25] Francisco de Melo Viríssimo, Adrian P. Martin, and Stephanie A. Henson. Influence of seasonal variability in flux attenuation on global organic carbon fluxes and nutrient distributions. *Global Biogeochemical Cycles*, 36(2):e2021GB007101, 2022.

[26] Lionel Guidi, Louis Legendre, Gabriel Reygondeau, Julia Uitz, Lars Stemmann, and Stephanie A. Henson. A new look at ocean carbon remineralization for estimating deepwater sequestration. *Global Biogeochemical Cycles*, 29(7):1044–1059, 2015.

[27] Sarah L. C. Giering, Richard Sanders, Adrian P. Martin, Stephanie A. Henson, Jennifer S. Riley, Chris M. Marsay, and David G. Johns. Particle flux in the oceans: Challenging the steady state assumption. *Global Biogeochemical Cycles*, 31(1):159–171, 2017.

[28] Samar Khatiwala. A computational framework for simulation of biogeochemical tracers in the ocean. *Global Biogeochemical Cycles*, 21(3), 2007.

[29] I. Kriest and A. Oschlies. Swept under the carpet: organic matter burial decreases global ocean biogeochemical model sensitivity to remineralization length scale. *Biogeosciences*, 10(12):8401–8422, 2013.

[30] D. Niemeyer, I. Kriest, and A. Oschlies. The effect of marine aggregate parameterisations on nutrients and oxygen minimum zones in a global biogeochemical model. *Biogeosciences*, 16(15):3095–3111, 2019.

[31] B. Pasquier, M. Holzer, M. A. Chamberlain, R. J. Matear, N. L. Bindoff, and F. W. Primeau. Optimal parameters for the ocean's nutrient, carbon, and oxygen cycles compensate for circulation biases but replumb the biological pump. *Biogeosciences*, 20(14):2985–3009, 2023.

[32] S.A. Henson, C. Laufkötter, S. Leung, S.L.C. Giering, H.I. Palevski, and E.L. Cavan. Uncertain response of ocean biological carbon export in a changing world. *Nature Geosciences*, 15:248–254, 2022.

[33] Jamie D. Wilson, Oliver Andrews, Anna Katavouta, Francisco de Melo Viríssimo, Ros M. Death, Markus Adloff, Chelsey A. Baker, Benedict Blackledge, Fraser W. Goldsworth, Alan T. Kennedy-Asser, Qian Liu, Katie R. Sieradzan, Emily Vosper, and Rui Ying. The biological carbon pump in cmip6 models: 21st century trends and uncertainties. *Proceedings of the National Academy of Sciences*, 119(29):e2204369119, 2022.

[34] O. Aumont, C. Ethé, A. Tagliabue, L. Bopp, and M. Gehlen. Pisces-v2: an ocean biogeochemical model for carbon and ecosystem studies. *Geoscientific Model Development*, 8(8):2465–2513, 2015.

[35] M. Vichi, N. Pinardi, and S. Masina. A generalized model of pelagic biogeochemistry for the global ocean ecosystem. part i: Theory. *Journal of Marine Systems*, 64(1):89–109, 2007. Contributions from Advances in Marine Ecosystem Modelling Research, 27-29 June, 2005, Plymouth, UK.

[36] Giorgio Dall'Olmo and Kjell Arne Mork. Carbon export by small particles in the norwegian sea. *Geophysical Research Letters*, 41(8):2921–2927, 2014.

[37] Nathan Briggs, Giorgio Dall'Olmo, and Hervé Claustre. Major role of particle fragmentation in regulating biological sequestration of CO_2 by the oceans. *Science*, 367(6479):791–793, 2020.

[38] Hervé Claustre, Kenneth S. Johnson, and Yuichiro Takeshita. Observing the global ocean with biogeochemical-argo. *Annual Review of Marine Science*, 12(1):23–48, 2020. PMID: 31433959.

[39] Robert J.W. Brewin, Shubha Sathyendranath, Trevor Platt, Heather Bouman, Stefano Ciavatta, Giorgio Dall'Olmo, James Dingle, Steve Groom, Bror Jönsson, Tihomir S. Kostadinov, Gemma Kulk, Marko Laine, Victor Martínez-Vicente, Stella Psarra, Dionysios E. Raitsos, Katherine Richardson, Marie-Hélène Rio, Cécile S. Rousseaux, Joe Salisbury, Jamie D. Shutler, and

Peter Walker. Sensing the ocean biological carbon pump from space: A review of capabilities, concepts, research gaps and future developments. *Earth-Science Reviews*, 217:103604, 2021.

[40] D. J. Clements, S. Yang, T. Weber, A. M. P. McDonnell, R. Kiko, L. Stemmann, and D. Bianchi. Constraining the particle size distribution of large marine particles in the global ocean with in situ optical observations and supervised learning. *Global Biogeochemical Cycles*, 36(5):e2021GB007276, 2022. e2021GB007276 2021GB007276.

[41] I. Kriest, S. Khatiwala, and A. Oschlies. Towards an assessment of simple global marine biogeochemical models of different complexity. *Progress in Oceanography*, 86(3):337 – 360, 2010.

[42] I. Kriest, A. Oschlies, and S. Khatiwala. Sensitivity analysis of simple global marine biogeochemical models. *Global Biogeochemical Cycles*, 26(2), 2012.

[43] Samar Khatiwala, Martin Visbeck, and Mark A. Cane. Accelerated simulation of passive tracers in ocean circulation models. *Ocean Modelling*, 9(1):51 – 69, 2005.

[44] Samar Khatiwala. samarkhatiwala/tmm: Version 2.0 of the transport matrix method software (2018, may 13). *Zenodo*, 2018.

[45] Francisco de Melo Viríssimo, Adrian P. Martin, Stephanie A. Henson, and Jamie D. Wilson. Model output used in the manuscript "Seasonal variability in particle flux attenuation in the global ocean generates spatial variability in annual transfer efficiency" (v1.0). *Zenodo*, 2023.

[46] Jacob A. Cram. Model output used in the manuscript "the role of particle size, ballast, temperature, and oxygen in the sinking flux to the deep sea". `https://bitbucket.org/ohnoplus/prism-transfer-efficiency`, 2018. Last checked on 08.01.2023.

[47] M. Hohenwarter, M. Borcherds, G. Ancsin, B. Bencze, M. Blossier, J. Éliás, K. Frank, L. Gál, A. Hofstätter, F. Jordan, Z. Konečný, Z. Kovács, E. Lettner, S. Lizelfelner, B. Parisse, C. Solyom-Gecse, C. Stadlbauer, and M. Tomaschko. GeoGebra 5.0.507.0, October 2018. `http://www.geogebra.org`.

[48] R. Pawlowicz. "M_Map: A mapping package for MATLAB", version 1.4m, [Computer software]. `www.eoas.ubc.ca/~rich/map.html`, 2020. Last checked on 08.01.2023.

SUPPLEMENTARY MATERIALS

SEASONALITY IN CARBON FLUX ATTENUATION EXPLAINS SPATIAL VARIABILITY IN TRANSFER EFFICIENCY

F. DE MELO VIRÍSSIMO[1,2,*], A. P. MARTIN[1], S. A. HENSON[1], J. D. WILSON[3,4]

[1] *National Oceanography Centre, Southampton, SO14 3ZH, United Kingdom*
[2] *Grantham Research Institute on Climate Change and the Environment, London School of Economics and Political Science, London, WC2A 2AE, United Kingdom*
[3] *School of Earth Sciences, University of Bristol, Bristol, BS8 1QU, United Kingdom*
[4] *Department of Earth, Ocean and Ecological Sciences, University of Liverpool, Liverpool, L69 3GP, United Kingdom*

NOTE: THIS IS A NON-PEER REVIEWED PREPRINT SUBMITTED TO EARTHARXIV

This PDF file includes:

- **Supplementary text**
- **Figures S.1 to S.13**
- **Tables S.1 to S.2**
- **SI References**

*Corresponding Author. e-mail: f.de-melo-virissimo@lse.ac.uk.

1 Constraining the seasonal cycle

In order to constrain the seasonal cycle, we leverage from an extensive dataset [1] containing a total of 897 estimates for the flux attenuation parameter, computed from flux observations at different locations and times between the years 1991-2012. Among the 897 estimates, 690 are in the Northern Hemisphere and 207 in the Southern Hemisphere. A global map showing the locations is presented in Figure S.1(a).

To better constrain the seasonal cycle, the data set was split between b values for the Northern and Southern Hemispheres. For the Southern (Northern, in parenthesis) Hemisphere, the data points were separated by season as below:

- **Summer (Winter)**: January, February March;
- **Autumn (Spring)**: April, May, June;
- **Winter (Summer)**: July, August, September;
- **Spring (Autumn)**: October, November, December.

For each season, we computed the following statistics: the average b, computed by taking an arithmetic mean over the corresponding dataset; and the spread of the data around the mean, measured using one (symmetric) standard deviation from the mean. The corresponding statistics are plotted in Figs. 1(a,b) (see main manuscript) and show a clear and consistent seasonal, co-sinusoidal pattern of highest attenuation in spring and lowest in autumn in both hemispheres, which allow us to approximate the seasonal cycle in each hemisphere as a cosine function shifted 3 months towards spring - see next section. This is also shown in Figure S.1(b), which in addition to the hemisphere-wise seasonal cycle, presents the average b in different ocean regions. Note that the latter is only illustrative, since some regions do not have enough data to resolve the seasonal cycle, but it helps to illustrate where mean hemisphere averages and uncertainties shown in Fig. 1 come from.

The spread of b values, presented in the main manuscript Fig. 1(c), show that most b values are between 0.5 and 2.0, which allow us to constrain the amplitude of the seasonal cycle (in our case, with respect to a reference mean value) - see next section.

Note that, because b comes from a nonlinear parameterisation (Equation (13)), the average b computed above does not equal the mean b value for that season - which can only be estimated through the export and transfer fluxes altogether.

2 Diagnostic model

The diagnostic model [2, 3] used in this study has been modified to include a seasonal cycle in the model's flux attenuation, which we denote by b^{model}, via the sinking speed as $w(z) = a \cdot z$ (m day^{-1}), where a (day^{-1}) is the sinking speed coefficient. This change alters the sinking speed such that $a = \lambda / b^{\text{model}}$ [2, 4] (see also Equations (8), (13) and (14) below).

The seasonal b^{model} is presented in Fig. S.2 and is mathematically given by

$$b^{\text{model}}(t, \phi) = 1.388 + \text{sign}(\phi) \cdot 0.6 \cdot \cos\left(2 \cdot \pi \cdot (t/T) + (\theta \cdot \pi/6)\right) \tag{1}$$

There, t corresponds to the time (in days) and $T = 360$ days. The number 1.388 corresponds to the optimal, original b^{model} in which the model is normally run. The value 0.6 is chosen so that b^{model} goes from about 0.5 to just above 2.0 across the year, therefore covering most of the observed values shown in Fig. 1(c), which is in line with the range of values reported in the literature [5]. The phase is taken to be $\theta = 3$ months, reflecting the maximum flux attenuation observed in spring, as explained in the previous section (see also Figs. 1(a,b)). This means that faster sinking (low attenuation) happens about 3 months after maximum growth as indicated in Fig. S.2(c). The variable ϕ corresponds to the latitude, which varies from -90° to 90°. Hence, the signal function sign(ϕ) is positive in the Northern Hemisphere, negative in the South, and zero† on the Equator. This means that, at each instant of time, the seasonal cycle is spatially homogeneous in each hemisphere.

The biogeochemical model is coupled to an offline version of the MITgcm 2.8° via the transport-matrix method (TMM) [6, 7, 8]. In addition to the well known advantages of using the TMM, this coupling allows one to easily turn off the circulation contribution to the detritus dynamics, which is necessary to properly assess the influence of seasonality in transfer efficiency.

All figures shown in this Supporting Information were generated from the model output available on Zenodo [9].

†Authors' convention.

2.1 Detritus modelling

Below the export zone z_0 (in this model set as z_0 =120m), the detritus pool is modelled as a passive tracer according to the following equation [2]

$$\frac{\partial}{\partial t}C(x,y,z,t) = \text{circulation} + \text{sinking} + \text{remineralisation}, \tag{2}$$

where $C(x,y,z,t)$ is the detritus concentration at a point (x,y,z) in space and at an instant t in time (days).

While the circulation component in Equation (2) is given by an advection-diffusion equation (plus eddy parameterisations) [10] that have been stored as a series of 12 transport matrices [6], both sinking and remineralisation components are modelled as below, following [2]:

$$\text{sinking} = \frac{\partial}{\partial z}\left(w(z)\cdot C(x,y,z,t)\right),$$

where $w(z)$ is the sinking speed (m day^{-1}),

$$\text{remineralisation} = -\left(\lambda \cdot C(x,y,z,t)\right).$$

where λ is the remineralisation rate (day^{-1}).

This leads to the following equation

$$\frac{\partial}{\partial t}C(x,y,z,t) = \text{circulation} + \frac{\partial}{\partial z}\left(w(z)\cdot C(x,y,z,t)\right) - \left(\lambda \cdot C(x,y,z,t)\right), \tag{3}$$

which is the general equation for detritus in this model [2].

2.2 Spinup and analytical solution

The model was spun up for 3,000 years to reach a consistently quasi-repeating annual cycle, a procedure that is consistent with the literature [2]. This means that, if C is the solution, then $C(x,y,z,t) = C(x,y,z,t+T)$, for any $t > 0$ after the model has been spun up, where the 1-year period in this model is given by $T = 360$ days. Hence,

$$\int_0^T \frac{\partial}{\partial t}C(x,y,z,t)dt = C(x,y,z,T) - C(x,y,z,0) = 0, \tag{4}$$

Note that, in general $\frac{\partial}{\partial t}C(x,y,z,t) \neq 0$ as the concentration is not stationary after (or during) spinup (as shown in previous studies [4]). The relationship above shows that it is the annual average after spinup that is stationary.

From the above, we are able to derive an analytical solution for the detritus concentration. If we ignore the circulation component and integrate both sides of Equation (3) over 1-year period T, the left-hand side will be zero, while the right-hand side will lead to an ordinary differential equation (ODE) to give $\overline{C}$. This can be solved analytically and the solution will be given by the Martin curve (see Equation (13)).

3 Revisiting particle flux and transfer efficiency

The POC transport at a location is usually quantified in terms of its molar flux F, which is given by the number of moles per unit time per unit area. Mathematically, we have

$$F(x,y,z,t) = w(z)\cdot C(x,y,z,t), \tag{5}$$

where C and w are the POC concentration and sinking speed, respectively. From now on, we shall omit the independent variables x and y (latitude and longitude, respectively) for simplicity, since all the analyses here are on depth z and time t.

The annual transfer efficiency TE, from the export depth z_0 to a depth $z > z_0$, is given by

$$\text{TE} = \frac{\overline{F(z,t)}}{\overline{F(z_0,t)}}, \tag{6}$$

where the overline denotes the 1-year average.

3.1 Seasonality as a source of spatial variability

If the sinking speed w does not depend on time, then

$$\overline{F(z,t)} = \left(\frac{1}{T}\right)\int_0^T w(z)\cdot C(z,t)dt = w(z)\cdot\left(\frac{1}{T}\right)\int_0^T C(z,t)dt = w(z)\cdot\overline{C(z,t)}. \quad (7)$$

meaning that the sinking speed and concentration are essentially decoupled in time. In other words, the mean of the product equals the product of the means.

In the absence of circulation, this implies an analytical solution to the flux of detritus and TE. In fact, ignoring circulation leads to

$$\frac{\partial}{\partial t}C(x,y,z,t) = \frac{\partial}{\partial z}\left(w(z)\cdot C(x,y,z,t)\right) - \left(\lambda\cdot C(x,y,z,t)\right),$$

If we integrate both sides of this equation over 1-year period T, we get

$$C(x,y,z,T) - C(x,y,z,0) = \frac{\partial}{\partial z}\left(w(z)\cdot\overline{C}(x,y,z,t)\right) - \left(\lambda\cdot\overline{C}(x,y,z,t)\right),$$

which combined with Equation (4) gives

$$\frac{\partial}{\partial z}\left(w(z)\cdot\overline{C}(x,y,z,t)\right) - \left(\lambda\cdot\overline{C}(x,y,z,t)\right) = 0.$$

The equation above can be rewritten as an ODE in z for $\overline{C}$, which has an analytical solution given by the Martin curve (see Equation (13)). Hence (see also Equation (14)),

$$\text{TE} = \frac{\overline{F(z,t)}}{\overline{F(z_0,t)}} = \frac{w(z)\cdot\overline{C(z,t)}}{w(z_0)\cdot\overline{C(z_0,t)}} = \left(\frac{z}{z_0}\right)^{-\lambda/a}. \quad (8)$$

Therefore, in the absence of circulation, the annual mean TE should be constant throughout the ocean, with the value given by Equation (8). This is illustrated in Fig. S.3 for the model's $-\lambda/a = b^{\text{model}} = 1.388$, where the export depth $z_0 = 120$m and the transfer depth z =1,080m. In these conditions, Equation (8) gives TE≈ 0.04738, in very good agreement with Fig. S.3.

The same does not happen if a (and hence the sinking speed) varies seasonally. In fact, if we suppose that $a = a(t)$, then $w = w(z,t) = a(t)\cdot z$ and hence the sinking speed cannot be taken out of the time-average integral in Equation (7). In other words, if w does depend on time, then

$$\overline{F(z,t)} = \left(\frac{1}{T}\right)\int_0^T w(z,t)\cdot C(z,t)dt = \overline{w(z,t)\cdot C(z,t)} \neq \overline{w(z,t)}\cdot\overline{C(z,t)}, \quad (9)$$

and the relationship in Equation (8) does not hold for $a = a(t)$.

This coupling between seasonality in sinking speed and seasonality in detritus concentration implies that, at each point in space (due to spatial variability in detritus concentration) and depth (due to the variability in time of the already sinking detritus), a different time series with different annual mean will emerge, hence leading to spatial variability in the flux ratios - and in particular in TE.

3.2 Examples

Examples illustrating the influence of seasonality in the detritus concentration and fluxes are provided in Fig. S.4 to Fig. S.8 for the South Atlantic, North Atlantic, South Pacific, North Pacific and Indian oceans, respectively. Fig.S.4(a) and Fig. S.4(b) are also shown in the main manuscript as Fig. 2(c) and Fig. 2(d), respectively.

4 Metrics computed

The local transfer efficiency TE at a point latitude x and longitude y is defined as

$$\text{TE}(x,y) = \frac{\overline{F}(x,y,z=1,080\text{m})}{\overline{F}(x,y,z=120\text{m})}. \quad (10)$$

The globally-integrated flux at a depth $z = z^*$m is given by

$$F_{z^*\text{m}} = \int_{(x,y)}\overline{F}(x,y,z=z^*\text{m})dxdy. \quad (11)$$

The global transfer efficiency can be computed as

$$\text{TE}_{\text{global}} = \frac{F_{1,080\text{m}}}{F_{120\text{m}}}, \tag{12}$$

where the export and transfer depth values of $z = 120$m and $z = 1,080$m respectively are imposed by the model as the depths where the diagnostic fluxes are evaluated.

Martin curve is given by

$$\overline{F}(x, y, z) = \overline{F}(x, y, z = z_0) \cdot \left(\frac{z}{z_0}\right)^{-b}, \tag{13}$$

where b is the flux attenuation parameter. In the conditions of Equation (7) and Equation (8), we have that $b = \lambda/a$.

From the Martin curve above, it follows that

$$\text{TE} = \frac{\overline{F}(x, y, z = 1,080\text{m})}{\overline{F}(x, y, 120\text{m})} = \left(\frac{z = 1,080\text{m}}{z = 120\text{m}}\right)^{-b}. \tag{14}$$

4.1 Mean temperature

Here we consider the annual mean of both surface (0-120m) and upper-mesopelagic (120-540m) ocean temperatures. These averages take into consideration the relative volume of each grid box and can be computed as

$$\text{Temp}_{\text{surf}}(x, y) = \left(\frac{1}{\text{Vol}_{\text{surf}}(x, y)}\right) \int_{z=0\text{m}}^{z=120\text{m}} \overline{\text{Temp}}(x, y, z)dz, \tag{15}$$

for the surface temperature, and

$$\text{Temp}_{\text{up-meso}}(x, y) = \left(\frac{1}{\text{Vol}_{\text{up-meso}}(x, y)}\right) \int_{z=120\text{m}}^{z=540\text{m}} \overline{\text{Temp}}(x, y, z)dz, \tag{16}$$

for the upper-mesopelagic temperature, where $\overline{\text{Temp}}(x, y, z)$ is the 1-year ocean mean temperature and

$$\text{Vol}_{\text{surf}}(x, y) = \int_{z=0\text{m}}^{z=120\text{m}} \text{Vol}(x, y, z)dz$$

is the volume of the surface water column at each point (x, y), with $\text{Vol}(x, y, z)$ being the volume of the grid box located at (x, y, z). The volume of the upper-mesopelagic water column, here denoted by $\text{Vol}_{\text{up-meso}}(x, y)$, can be computed in a similar fashion.

4.2 Province division

The division of the ocean into zones (or provinces) used here is similar to that adopted in previous studies [11] and is based on the annual mean of the upper-mesopelagic ocean temperature as main indicator, as well as latitude and longitude. The division is described below, and the result is shown in Fig. S.9.

- Antactic Zone (AAZ): $\text{Temp}_{\text{up-meso}}(x, y) < 4$ and Latitude $< 45°$ S.
- Subantarctic Zone (SAZ): $4 \leq \text{Temp}_{\text{up-meso}}(x, y) < 13.5$ and Latitude $< 35°$ S.
- North Pacific (NP): $4 \leq \text{Temp}_{\text{up-meso}}(x, y) < 13.5$ and Latitude $> 25°$ N and Longitude $< 280°$ E.
- North Atlantic (NA): $-10 \leq \text{Temp}_{\text{up-meso}}(x, y) < 13.5$ and Latitude $> 25°$ N and Longitude $< 100°$ E and Longitude $> 250°$ E.
- Eastern Tropical Atlantic (ETA): $4 \leq \text{Temp}_{\text{up-meso}}(x, y) < 13.5$ and $35° <$ S Latitude $< 25°$ N and Longitude $< 50°$ E and Longitude $> 300°$ E.
- Eastern Tropical Pacific (ETP): $4 \leq \text{Temp}_{\text{up-meso}}(x, y) < 13.5$ and $35° <$ S Latitude $< 25°$ N and $50° <$ E Longitude $< 300°$ E.
- Subtropical Pacific (STP): $\text{Temp}_{\text{up-meso}}(x, y) \geq 13.5$ and Longitude $< 274.2°$ E.
- Subtropical Atlantic (STA): $\text{Temp}_{\text{up-meso}}(x, y) \geq 13.5$ and Longitude $> 274.2°$ E.

4.3 Flux profiles

The annual flux profile in each province X is computed as the average flux across the province as below

$$F_{\text{provinceX}}(z) = \left(\frac{1}{\text{Area}_{\text{provinceX}}(z)}\right) \int_{(x,y)} \overline{F}(x,y,z)dxdy, \tag{17}$$

where $\text{Area}_{\text{provinceX}}(z)$ is the area of the province at each depth z. These fluxes are then used to compute TE at each province using the equation above. This is shown in Fig. 1(c) in the main manuscript.

4.4 Assumptions

In all the above, we only use model output where the water depth is at least 1,080m deep. This excludes shallow areas such as shelves and coastal locations, but including them would introduce a significant bias to the export fluxes relative to the deep ocean transfer flux.

5 Reproducing Henson et al. (2012)

The Henson et al. (2012) [12] data compilation included global flux data at 41 locations spanning several regions of the world. These locations, however, are mostly concentrated in the Southern Ocean (below 45°S), Tropical areas (15°N-15°S), and both Northern Atlantic and Pacific oceans. These fluxes differ in date and sampling duration, and also in the methodology used to estimate them. The export fluxes (100m ± 20m) are Thorium-derived, and in high latitudes were collected mostly in summer months while those in the tropics where collected all through the year. The deep ocean fluxes (2,000m) are annual mean based on deep-ocean sediment trap data, collected at different depths and extrapolated to 2,000m via the Martin curve with $b = 0.86$. The transfer efficiency is then calculated using these annually-averaged deep ocean fluxes divided by the short-duration export fluxes, with the results being extrapolated to the rest of the ocean via a relation with sea surface temperature data from satellite.

To compute TE according to the methodology of Henson et al. (2012) [12], we randomly sampled 150 points (50 at each region below) from the aforementioned areas as follows:

- **Southern latitudes** (below 45°S): average over summer months (January-March) and computed TE at 50 randomly sampled locations;
- **Northern latitudes** (above 45°N): average over summer months (July-August) and computed TE at 50 randomly sampled locations;
- **Tropical latitudes** (15°N-15°S): average over the entire year and computed TE at 50 randomly sampled locations.

The same procedure was followed to compute the 1-year average surface temperature (120m-540m) at each sampled location. An example of this sampling is shown in Fig. S.10(a).

We then performed both linear and nonlinear (exponential) regressions of this sampled TE and surface temperature data $\text{Temp}_{\text{surf}}$, as shown in Fig. S.11(b) and Fig. S.12(b) respectively. These are based on the following equations for TE as a function of $\text{Temp}_{\text{surf}}$:

$$\text{TE} = \alpha_{\text{linear}} \cdot \text{Temp}_{\text{surf}} + \beta_{\text{linear}}.$$

and

$$\text{TE} = \alpha_{\text{exp}} \cdot \left(e^{\beta_{\text{exp}} \cdot (\text{Temp}_{\text{surf}} - \text{Temp}_{\text{ref}})}\right) + \text{TE}_{\text{ref}},$$

where $\alpha_{\text{linear}}, \beta_{\text{linear}}$ and $\alpha_{\text{exp}}, \beta_{\text{exp}}$ are the parameters to be fitted in the linear and nonlinear regressions respectively. There, we chose $\text{Temp}_{\text{ref}} = 20$ and $\text{TE}_{\text{ref}} = 0.035$, which are based on the range of observed TE and surface temperature observed in the sampled model data.

To quantify the uncertainty, we repeated this procedure 10,000 times, with results shown in Table S.1 and the left column of Figs. S.10, S.11. This resulted in the following regression relationships:

$$\text{TE} = 0.0017 \cdot \text{Temp}_{\text{surf}} + 0.0419, \tag{18}$$

$$\text{TE} = 0.0373 \cdot \left(e^{0.0624 \cdot (\text{Temp}_{\text{surf}} - 20)}\right) + 0.035. \tag{19}$$

We then used these relationships to infer the TE profiles, as shown in Figs. S.10(c) and S.11(c) for the linear and exponential parameterisations respectively. These are consistent with Henson et al. (2012) [12], showing TE that is higher at low latitudes and low at high latitudes.

We attempted the same experiment using the upper-mesopelagic temperature $\mathrm{Temp}_{\mathrm{up-meso}}$ instead of the surface temperature. For that, we chose $\mathrm{Temp}_{\mathrm{ref}} = 14$ and $\mathrm{TE}_{\mathrm{ref}} = 0.042$, which again are based on the range of observed TE and surface temperature observed in the sampled model data. The procedure results are shown in Table S.2, and illustrated in Figs. S.12, S.13 for both linear and nonlinear regression, respectively. The relationships obtained are

$$\mathrm{TE} = 0.0028 \cdot \mathrm{Temp}_{\mathrm{up-meso}} + 0.0406. \tag{20}$$

$$\mathrm{TE} = 0.0378 \cdot \left(e^{0.1620 \cdot \left(\mathrm{Temp}_{\mathrm{up-meso}} - 14\right)} \right) + 0.042, \tag{21}$$

which correspond to the TE maps shown in Fig. S.12(c) and Fig. S.13(c). Although slightly different, these TE maps also show a high latitude-low TE, low-latitude-high TE pattern, again highlighting the bias introduced by selective sampling of flux data in a context of seasonality in flux attenuation.

References

[1] Lionel Guidi, Louis Legendre, Gabriel Reygondeau, Julia Uitz, Lars Stemmann, and Stephanie A. Henson. A new look at ocean carbon remineralization for estimating deepwater sequestration. *Global Biogeochemical Cycles*, 29(7):1044–1059, 2015.

[2] I. Kriest, S. Khatiwala, and A. Oschlies. Towards an assessment of simple global marine biogeochemical models of different complexity. *Progress in Oceanography*, 86(3):337 – 360, 2010.

[3] I. Kriest, A. Oschlies, and S. Khatiwala. Sensitivity analysis of simple global marine biogeochemical models. *Global Biogeochemical Cycles*, 26(2), 2012.

[4] Francisco de Melo Viríssimo, Adrian P. Martin, and Stephanie A. Henson. Influence of seasonal variability in flux attenuation on global organic carbon fluxes and nutrient distributions. *Global Biogeochemical Cycles*, 36(2):e2021GB007101, 2022.

[5] E. Kwon, F. Primeau, and J. Sarmiento. The impact of remineralization depth on the air–sea carbon balance. *Nature Geosciences*, 2:630–635, 2009.

[6] Samar Khatiwala, Martin Visbeck, and Mark A. Cane. Accelerated simulation of passive tracers in ocean circulation models. *Ocean Modelling*, 9(1):51 – 69, 2005.

[7] Samar Khatiwala. A computational framework for simulation of biogeochemical tracers in the ocean. *Global Biogeochemical Cycles*, 21(3), 2007.

[8] Samar Khatiwala. samarkhatiwala/tmm: Version 2.0 of the transport matrix method software (2018, may 13). *Zenodo*, 2018.

[9] Francisco de Melo Viríssimo, Adrian P. Martin, Stephanie A. Henson, and Jamie D. Wilson. Model output used in the manuscript "Seasonal variability in particle flux attenuation in the global ocean generates spatial variability in annual transfer efficiency" (v1.0). *Zenodo*, 2023.

[10] Jorge L. Sarmiento and Nicolas Gruber. *Ocean Biogeochemical Dynamics.* Princeton University Press, 2006.

[11] Thomas Weber, Jacob A. Cram, Shirley W. Leung, Timothy DeVries, and Curtis Deutsch. Deep ocean nutrients imply large latitudinal variation in particle transfer efficiency. *Proceedings of the National Academy of Sciences*, 113(31):8606–8611, 2016.

[12] Stephanie A. Henson, Richard Sanders, and Esben Madsen. Global patterns in efficiency of particulate organic carbon export and transfer to the deep ocean. *Global Biogeochemical Cycles*, 26(1), 2012.

Table S.1: Statistics for TE versus surface temperature linear regression in Equation (18), and for nonlinear (exponential) regression in Equation (19), both from 10,000 random samples, p-value < 0.005.

regression parameters	R^2_{linear}	α_{linear}	β_{linear}	R^2_{exp}	α_{exp}	β_{exp}
μ (mean)	0.7878	0.0017	0.0419	0.7978	0.0373	0.0624
σ (variance)	0.0308	7.2815e-05	6.6336e-04	0.0335	0.0010	0.0024

Table S.2: Statistics for TE versus upper-mesopelagic temperature linear regression in Equation (20), and for nonlinear (exponential) regression in Equation (21), both from 10,000 random samples, p-value < 0.005.

regression parameters	R^2_{linear}	α_{linear}	β_{linear}	R^2_{exp}	α_{exp}	β_{exp}
μ (mean)	0.7326	0.0028	0.0406	0.7807	0.0378	0.1620
σ (variance)	0.0286	1.0957e-04	6.4315e-04	0.0294	0.0015	0.0067

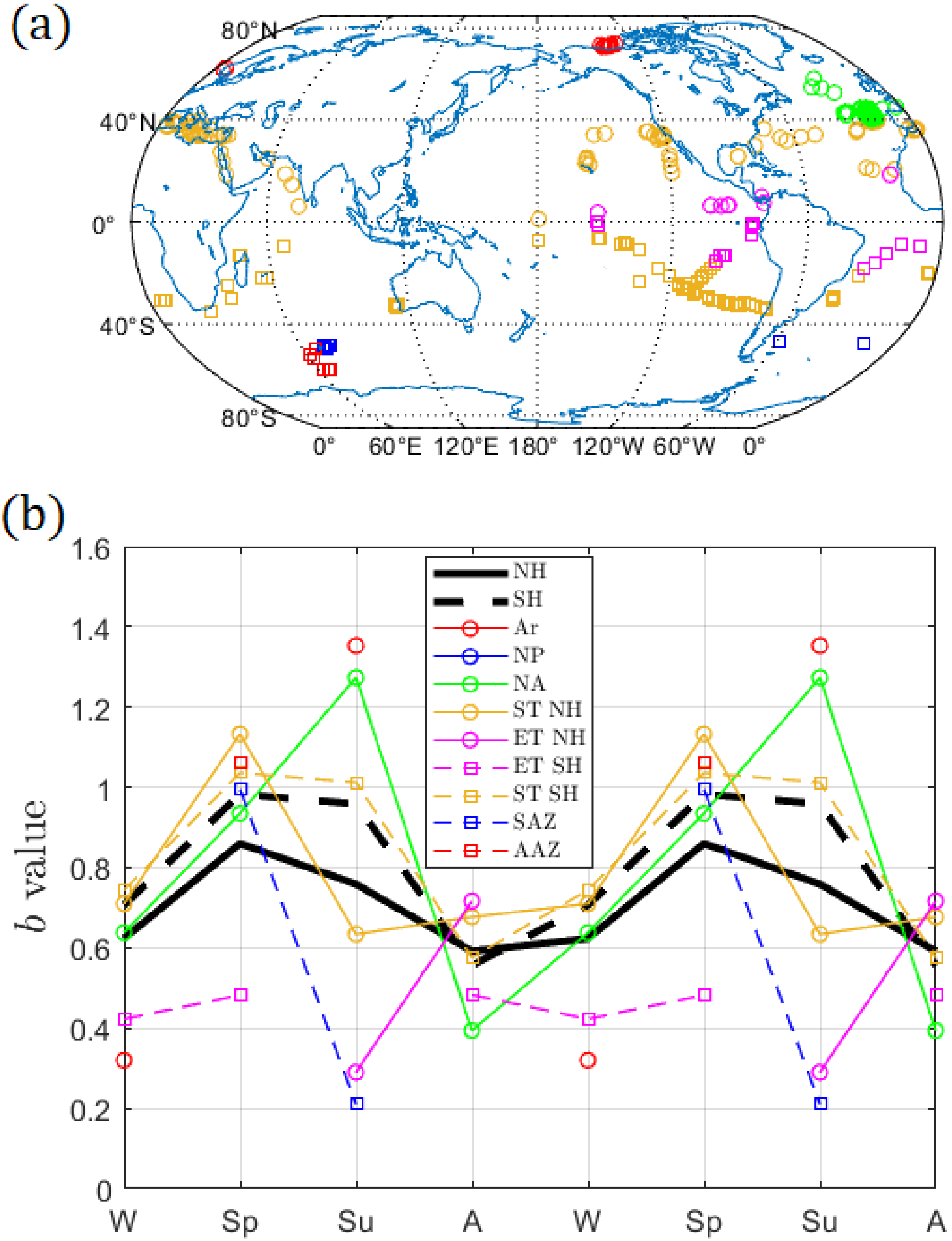

Figure S.1: Constraining the seasonal cycle in the flux attenuation parameter b in each hemisphere from the dataset [1]. Top: (a) Geographical location of the sampled data [1]. Different colours corresponds to different ocean regions. Bottom: (b) Seasonally averaged flux attenuation parameter b in different hemispheres and regions. The Northern (NH) and Southern (SH) Hemispheres are indicated by the solid and dashed black lines, respectively. Northern Hemisphere Arctic (Ar), North Pacific (NP), North Atlantic (NA), Subtropical (ST) and Tropical (ET) regions are shown in coloured circles (interpolated by solid lines) and Southern Hemisphere regions ET, ST, South Atlantic (SAZ) and Antarctic (AAZ) in coloured squares (interpolated by dashed lines).

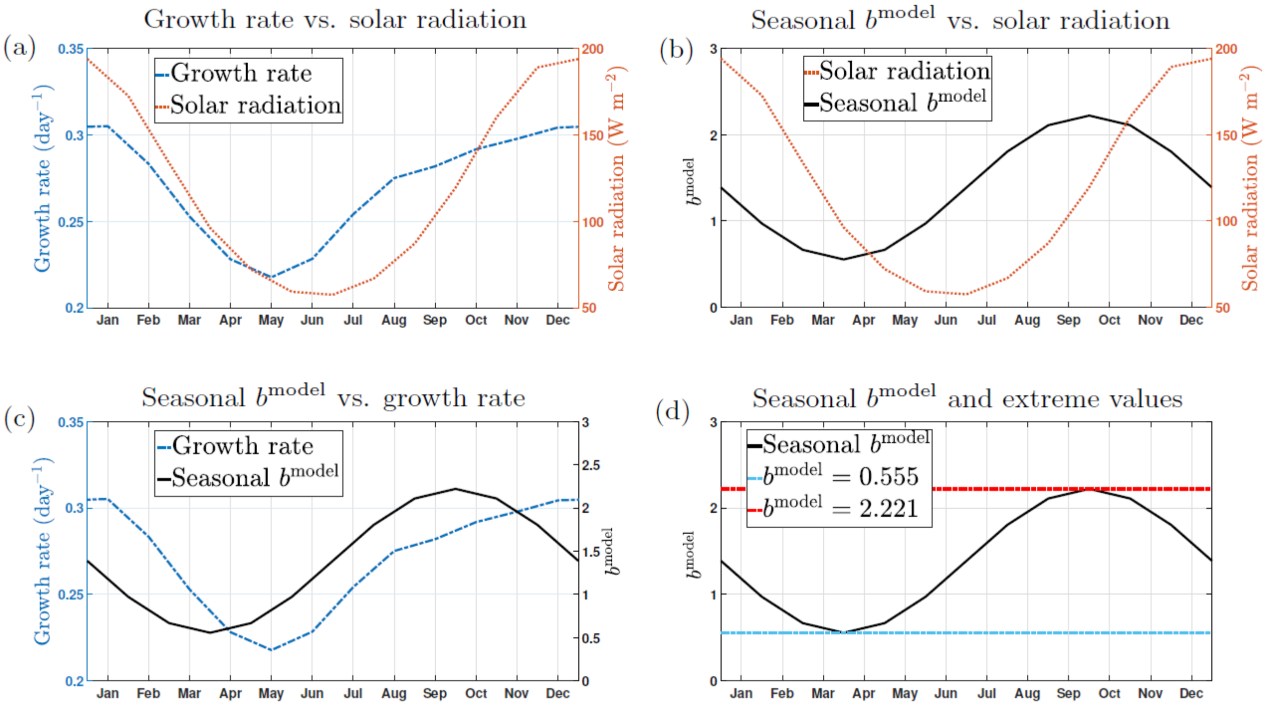

Figure S.2: Seasonal b^{model} in the Southern Hemisphere. Top: (a) Growth rate vs. solar radiation; (b) Seasonal b^{model} vs. solar radiation. Bottom: (c) Seasonal b^{model} vs. growth rate; (d) Seasonal b^{model} and extreme values. Versions of (a) and (b) also appear in de Melo Viríssimo et al. (2022) [4]

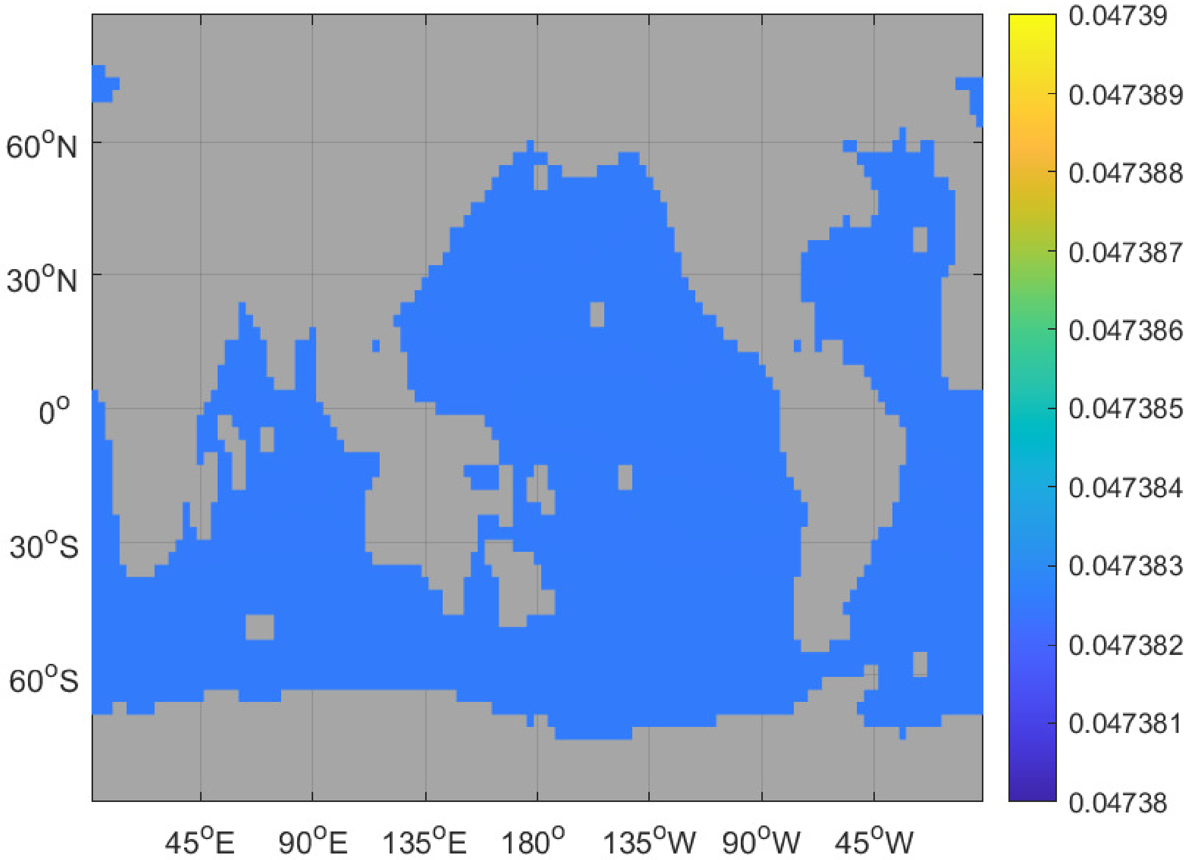

Figure S.3: Annual mean TE for a non-seasonal, constant $b^{model} = 1.388$. A version of this figure also appear in de Melo Viríssimo et al. (2022) [4]

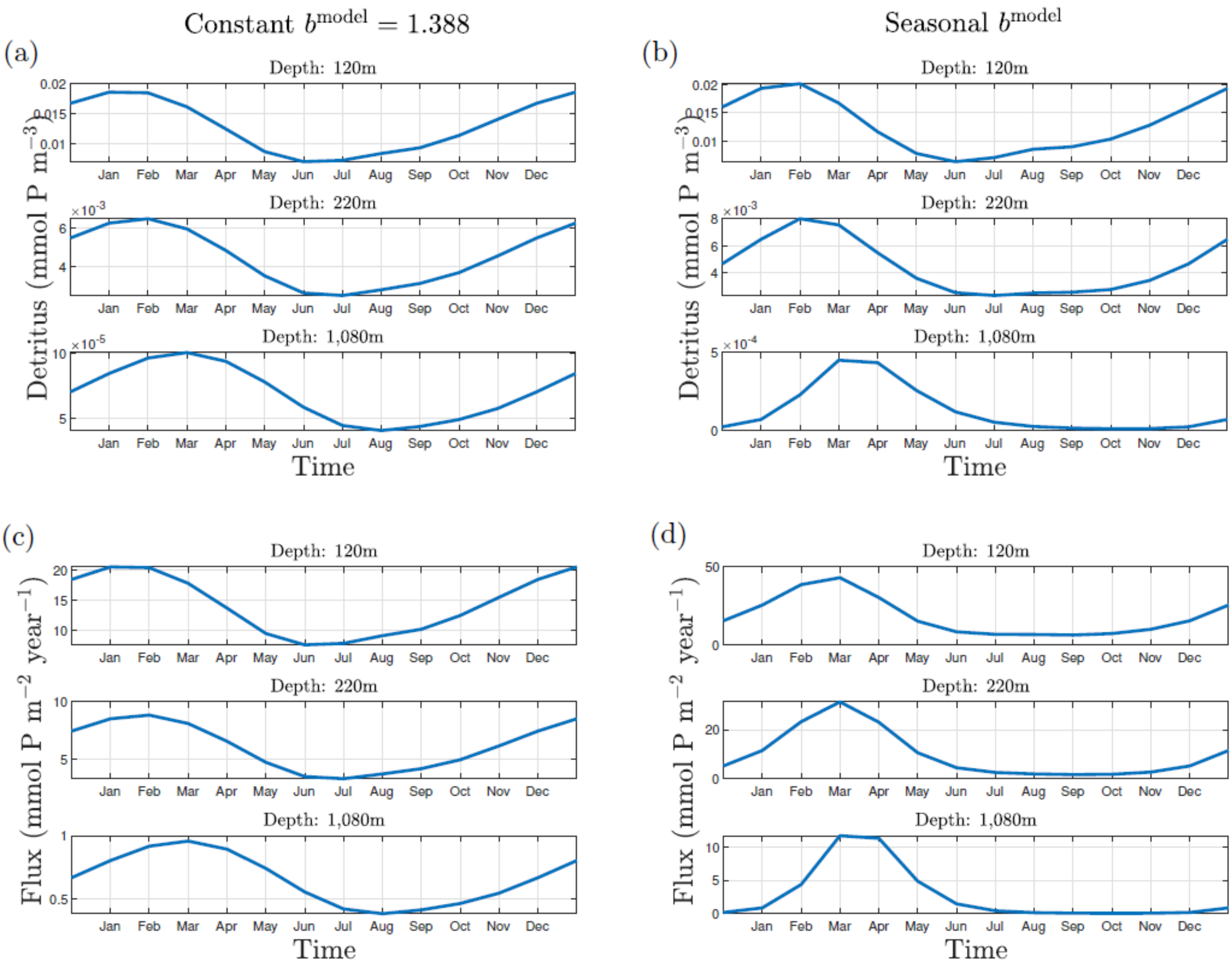

Figure S.4: Exported detritus attenuation in constant and seasonal attenuation scenarios, when detritus is not transported by the ocean circulation. Top: time series for detritus concentration in the South Atlantic Ocean (43.59°S, 29.53°W) at different depths TE for (a) a constant $b^{\text{model}} = 1.388$ and (b) a seasonal b^{model}. Bottom: time series for detritus flux for (c) $b^{\text{model}} = 1.388$ and (d) a seasonal b^{model}.

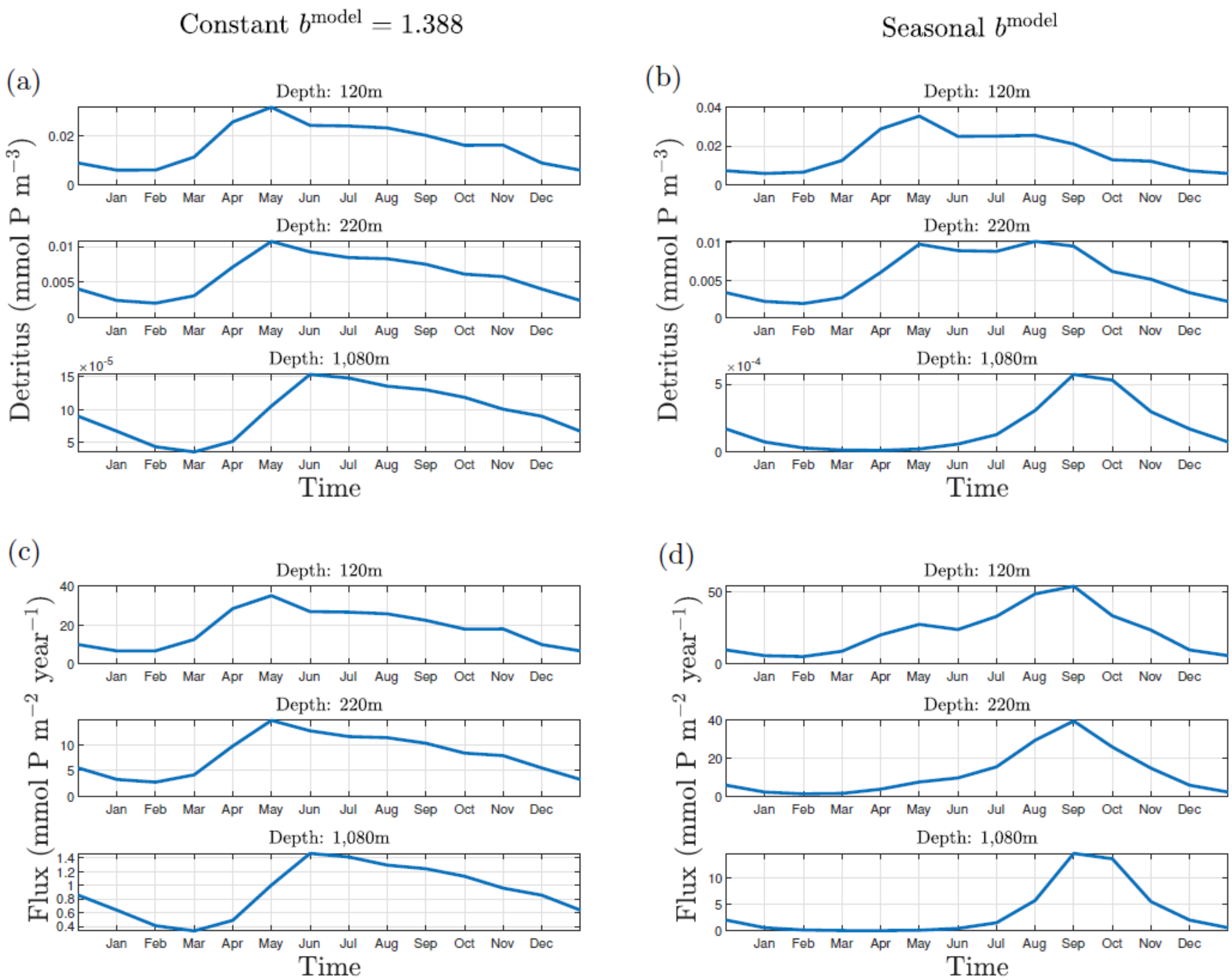

Figure S.5: Exported detritus attenuation in constant and seasonal attenuation scenarios, when detritus is not transported by the ocean circulation. Top: time series for detritus concentration in the North Atlantic Ocean (43.59°N, 35.52°W) at different depths for (a) a constant $b^{\text{model}} = 1.388$ and (b) a seasonal b^{model}. Bottom: time series for detritus flux for (c) $b^{\text{model}} = 1.388$ and (d) a seasonal b^{model}.

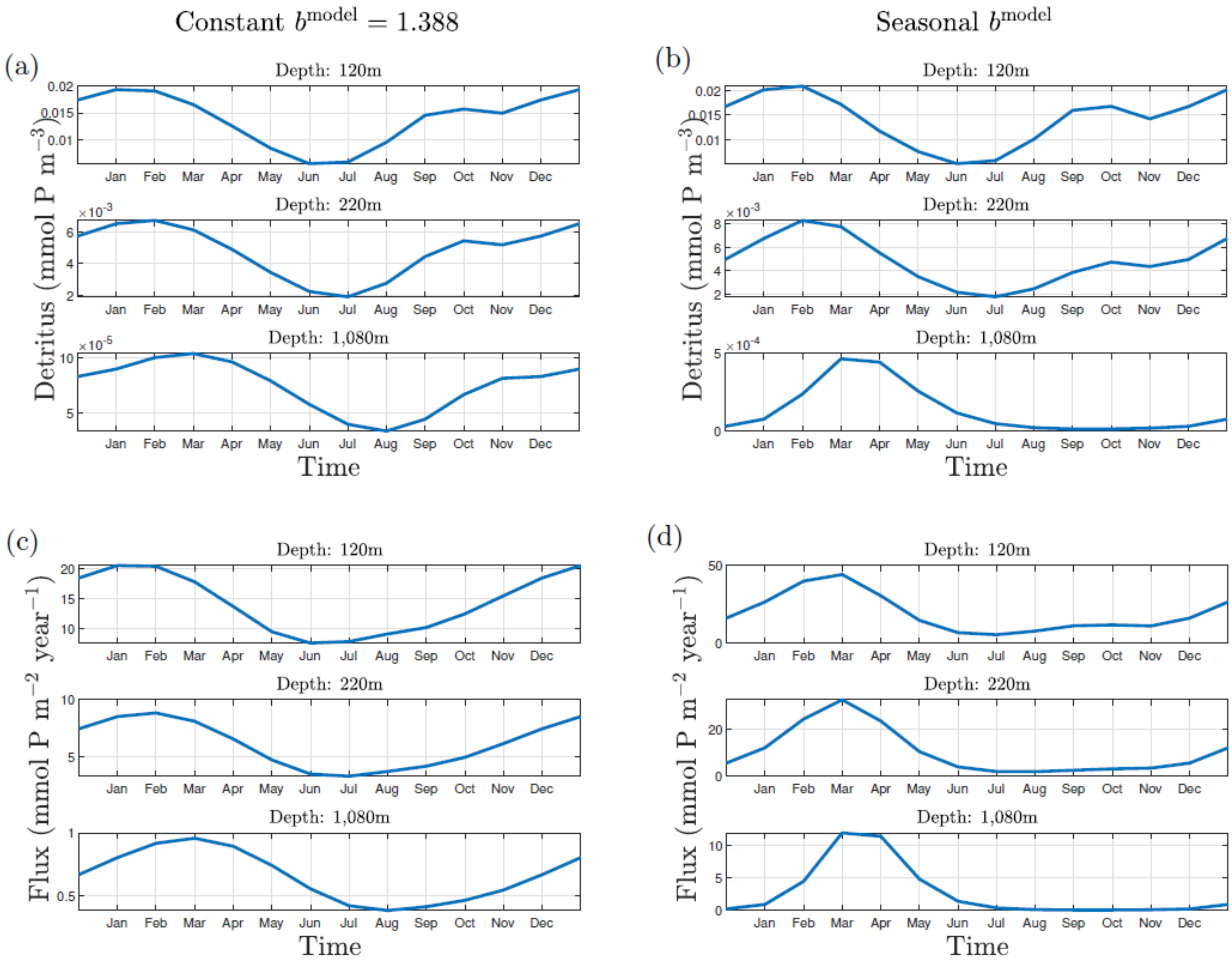

Figure S.6: Exported detritus attenuation in constant and seasonal attenuation scenarios, when detritus is not transported by the ocean circulation. Top: time series for detritus concentration in the South Pacific Ocean (46.41°S, 150.47°W) at different depths TE for (a) a constant $b^{\text{model}} = 1.388$ and (b) a seasonal b^{model}. Bottom: time series for detritus flux for (c) $b^{\text{model}} = 1.388$ and (d) a seasonal b^{model}.

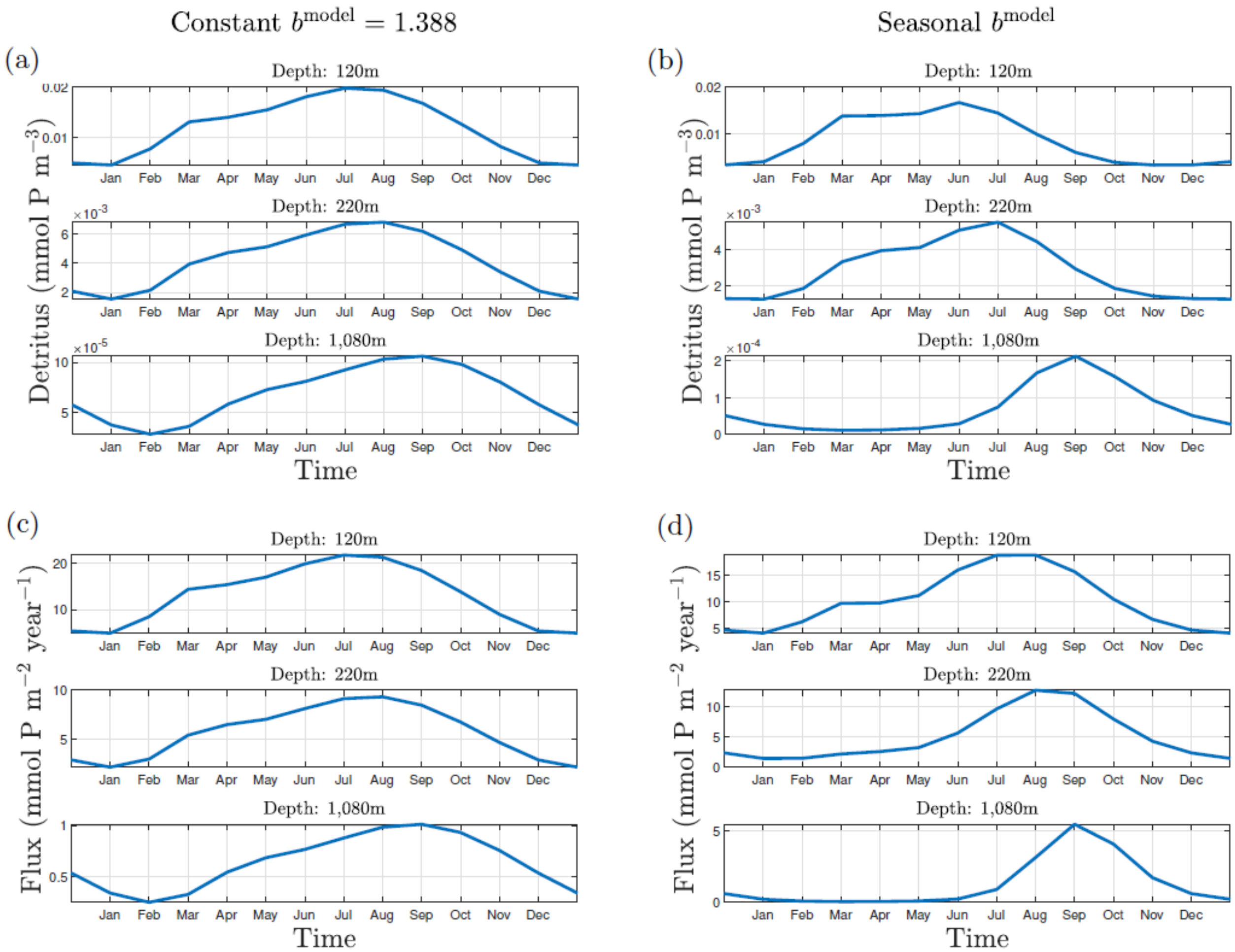

Figure S.7: Exported detritus attenuation in constant and seasonal attenuation scenarios, when detritus is not transported by the ocean circulation. Top: time series for detritus concentration in the North Pacific Ocean (49.21°N, 136.41°W) at different depths TE for (a) a constant $b^{\mathrm{model}} = 1.388$ and (b) a seasonal b^{model}. Bottom: time series for detritus flux for (c) $b^{\mathrm{model}} = 1.388$ and (d) a seasonal b^{model}.

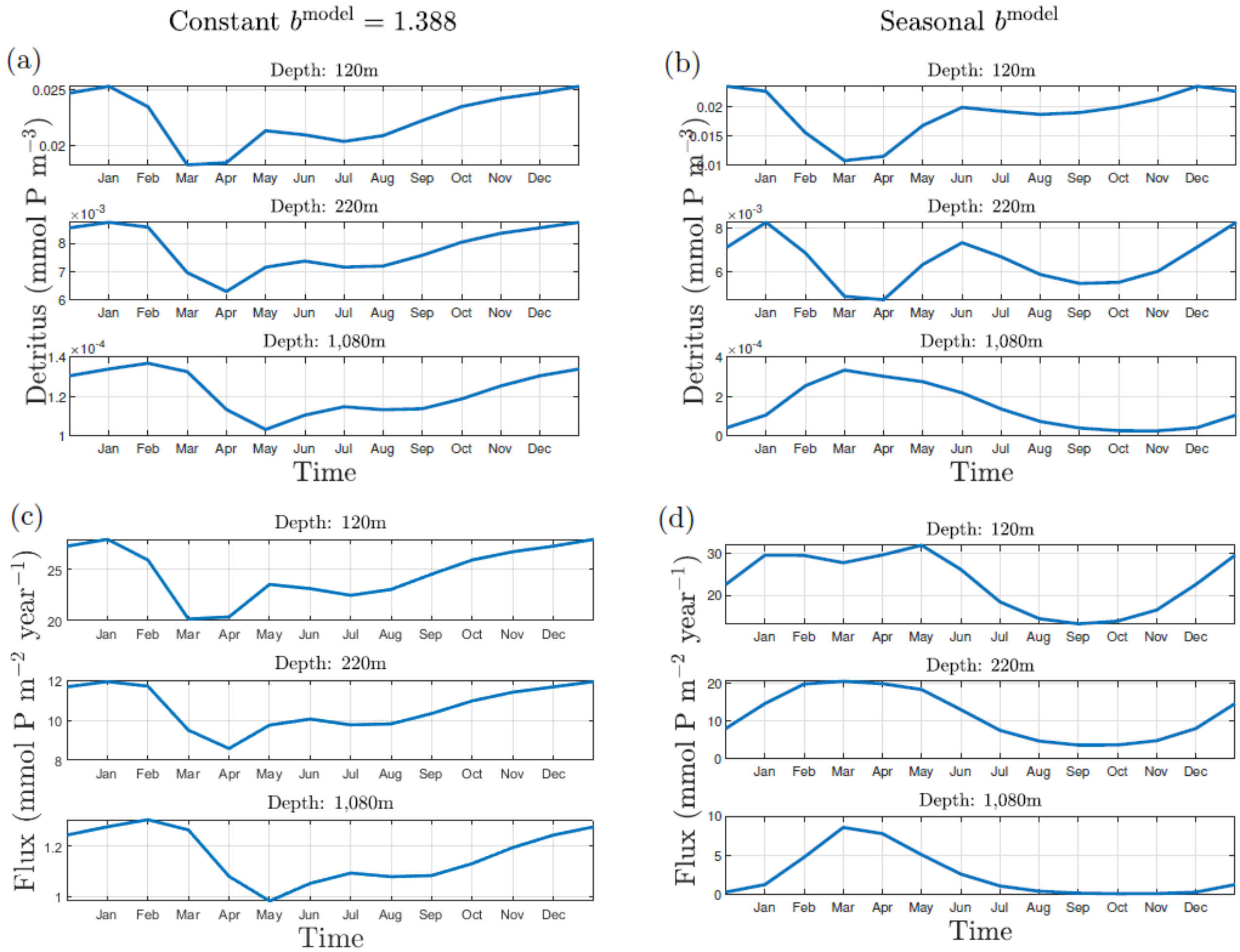

Figure S.8: Exported detritus attenuation in constant and seasonal attenuation scenarios, when detritus is not transported by the ocean circulation. Top: time series for detritus concentration in the Indian Ocean (7.03°S, 74.53°E) at different depths TE for (a) a constant $b^{\text{model}} = 1.388$ and (b) a seasonal b^{model}. Bottom: time series for detritus flux for (c) $b^{\text{model}} = 1.388$ and (d) a seasonal b^{model}.

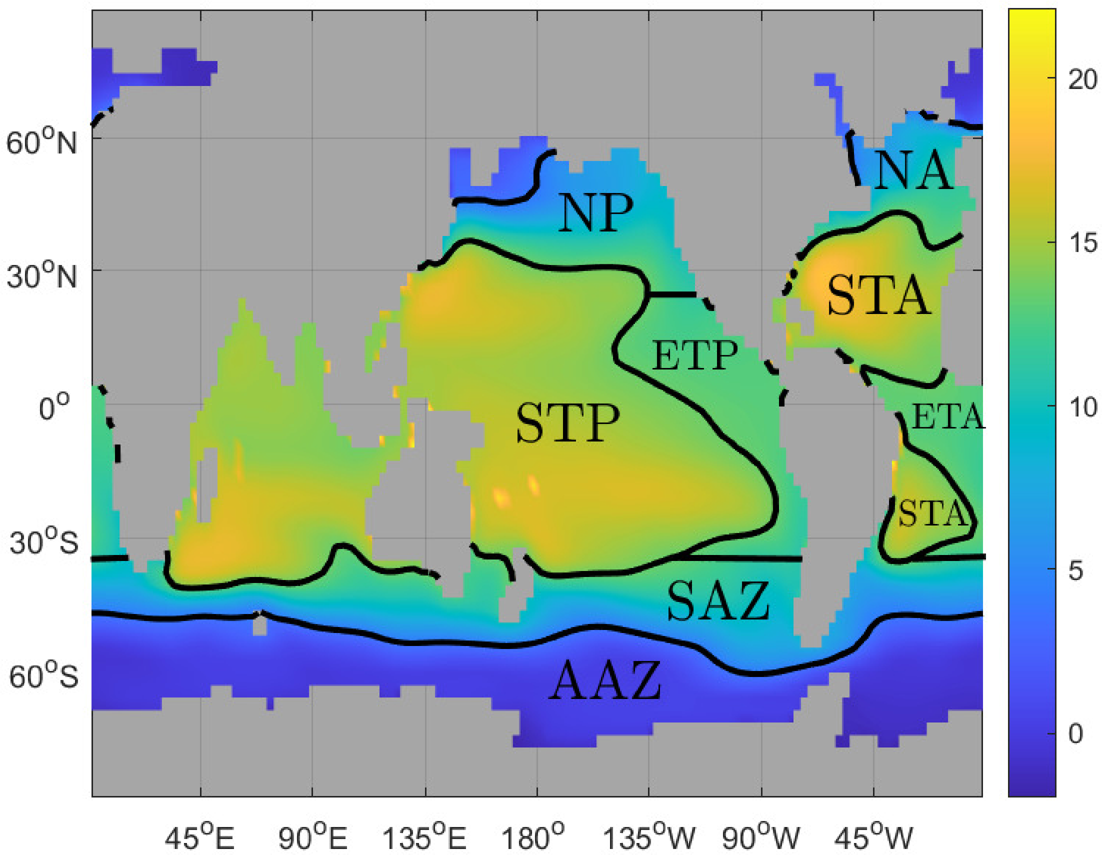

Figure S.9: Annual mean upper-mesopelagic temperature (in °C) with ocean provinces.

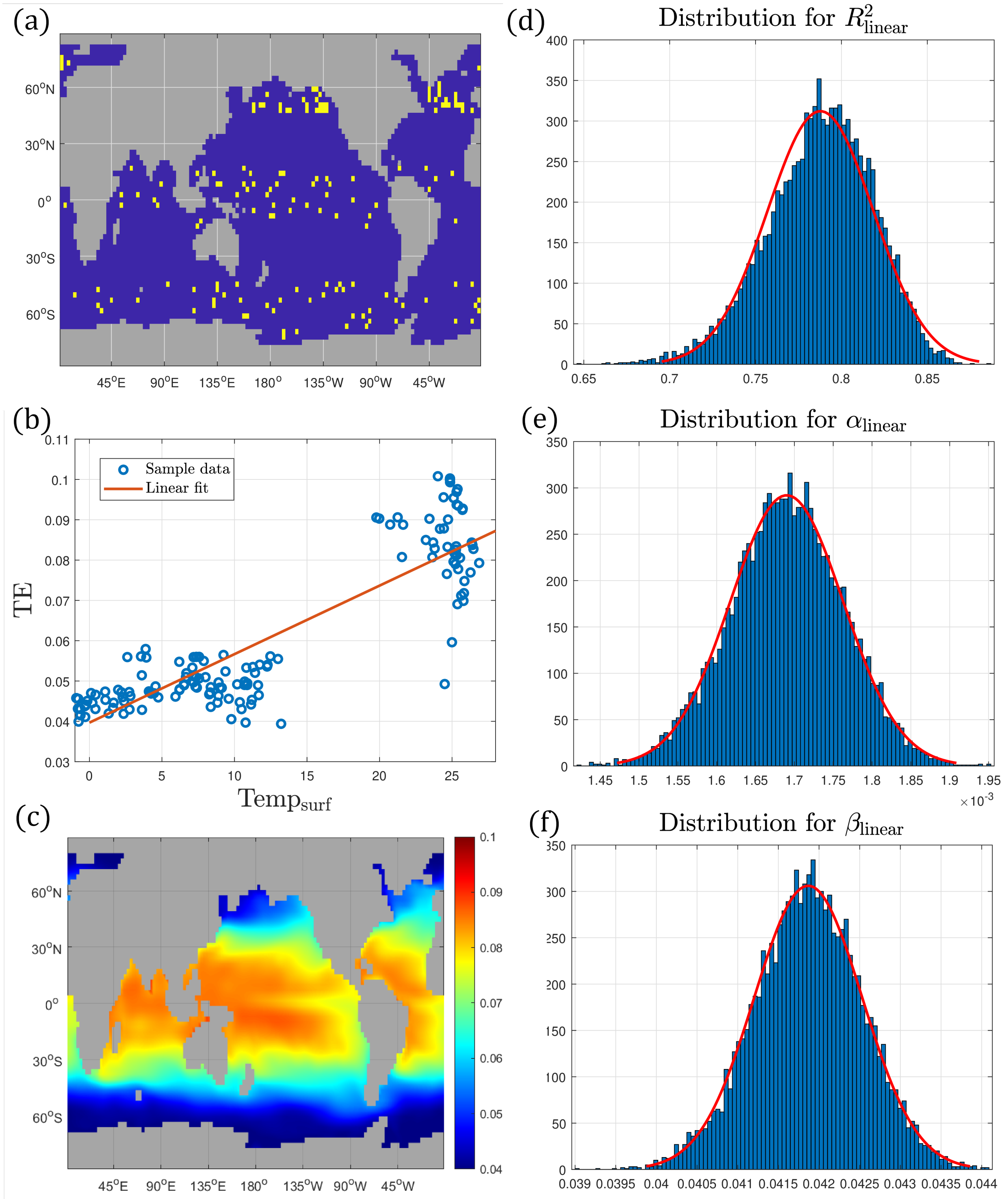

Figure S.10: Annual mean TE obtained from linear regression using surface (top 120m) temperature Temp$_{\text{surf}}$, based on Equation (18), which follows the procedure of Henson et al. (2012). Right column illustrates their procedure: (a) Example of randomly sampled locations (from within the 3 areas sampled by Henson et al. (2012) [12]) from model data; (b) Example of linear statistical regression using the random sample from model data in (a); (c) Annual mean TE given by the linear fit. Left column shows the histograms for 10,000 random samples: (d) Distribution for R^2_{linear}; (e) Distribution for α_{linear}; (f) Distribution for β_{linear}.

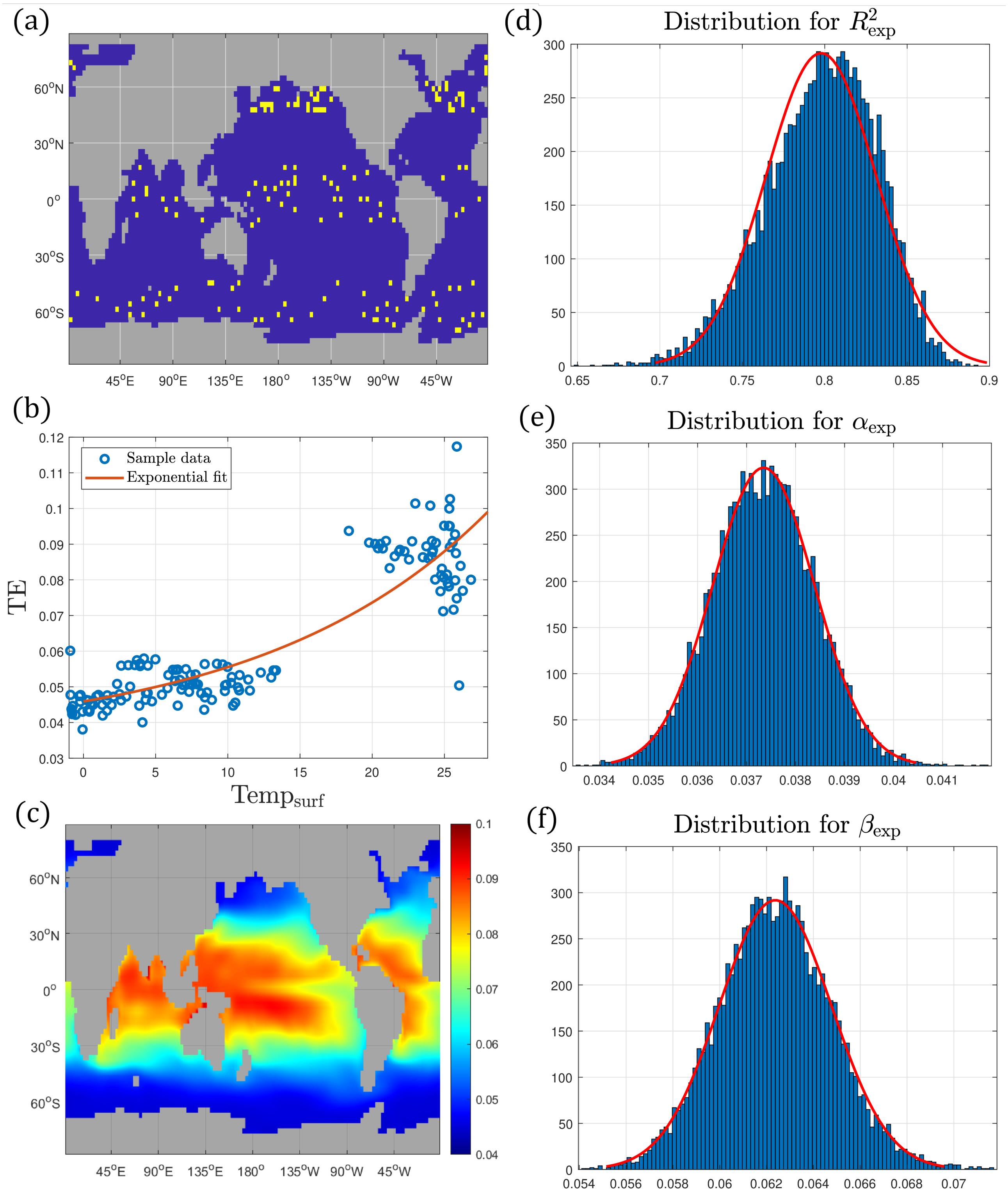

Figure S.11: Annual mean TE obtained from nonlinear (exponential) regression using surface (top 120m) temperature $\mathrm{Temp_{surf}}$, based on Equation (19), which follows the procedure of Henson et al. (2012). Right column illustrates their procedure: (a) Example of randomly sampled locations (from within the 3 areas sampled by Henson et al. (2012) [12]) from model data; (b) Example of nonlinear statistical regression using the random sample from model data in (a); (c) Annual mean TE given by the nonlinear fit. Left column shows the histograms for 10,000 random samples: (d) Distribution for $R^2_{\exp}$; (e) Distribution for $\alpha_{\exp}$; (f) Distribution for $\beta_{\exp}$.

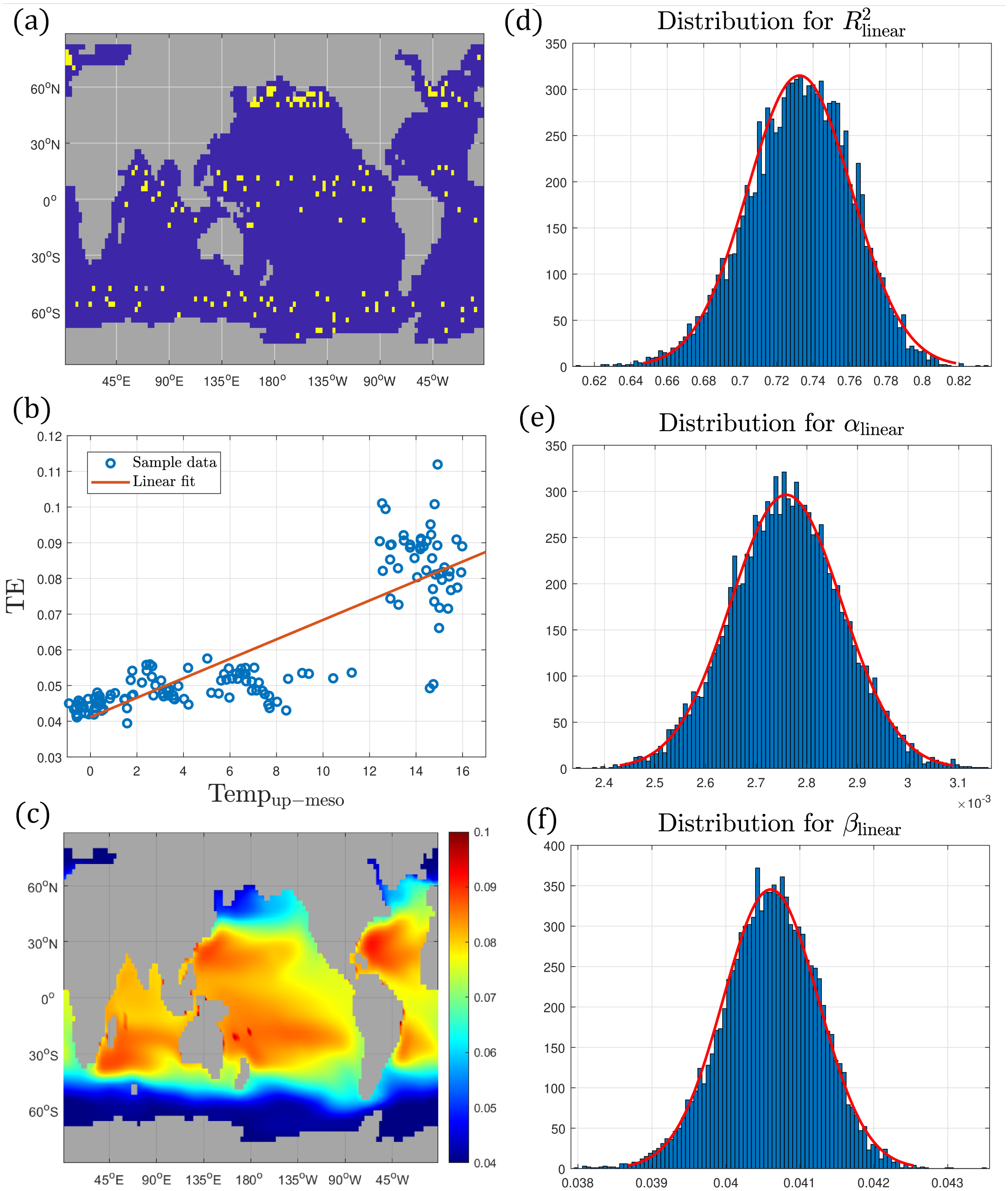

Figure S.12: Annual mean TE obtained from linear regression using upper-mesopelagic (120-540m) temperature Temp$_{\text{up-meso}}$, based on Equation (20), which follows the procedure of Henson et al. (2012). Right column illustrates their procedure: (a) Example of randomly sampled locations (from within the 3 areas sampled by Henson et al. (2012) [12]) from model data; (b) Example of linear statistical regression using the random sample from model data in (a); (c) Annual mean TE given by the linear fit. Left column shows the histograms for 10,000 random samples: (d) Distribution for R^2_{linear}; (e) Distribution for α_{linear}; (f) Distribution for β_{linear}.

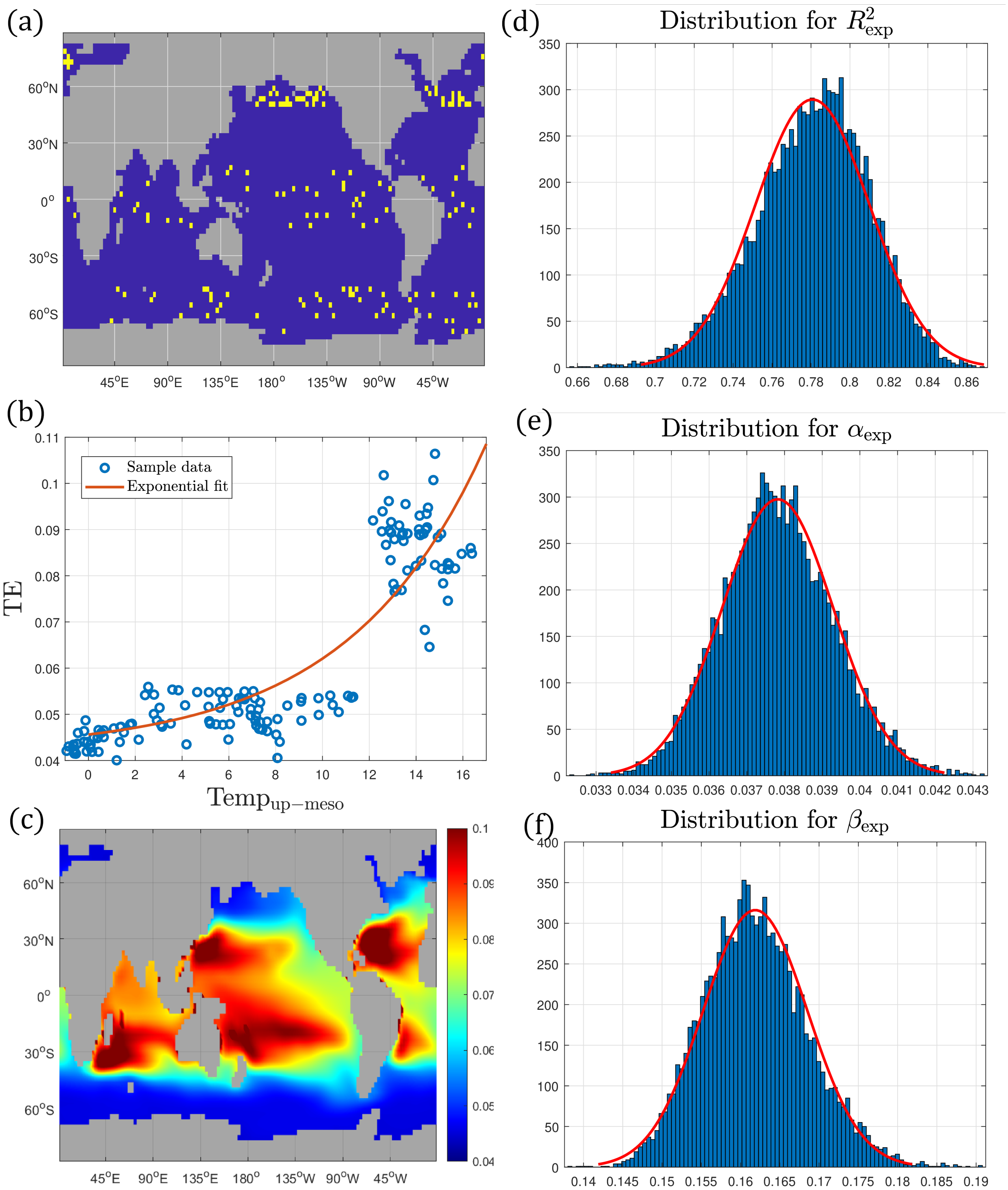

Figure S.13: Annual mean TE obtained from nonlinear (exponential) regression using surface (top 120m) temperature Temp$_{\text{up-meso}}$, based on Equation (21), which follows the procedure of Henson et al. (2012). Right column illustrates their procedure: (a) Example of randomly sampled locations (from within the 3 areas sampled by Henson et al. (2012) [12]) from model data; (b) Example of nonlinear statistical regression using the random sample from model data in (a); (c) Annual mean TE given by the nonlinear fit. Left column shows the histograms for 10,000 random samples: (d) Distribution for R^2_{exp}; (e) Distribution for α_{exp}; (f) Distribution for β_{exp}.